4-2009

Transmission and Guiding of Fast Electrons through Insulating Nanocapillaries and Comparison with Ion Guiding

Susanta Das
Western Michigan University

TRANSMISSION AND GUIDING OF FAST ELECTRONS THROUGH INSULATING NANOCAPILLARIES AND COMPARISON WITH ION GUIDING

by

Susanta Das

A Dissertation
Submitted to the
Faculty of The Graduate College
in partial fulfillment of the
requirements for the
Degree of Doctor of Philosophy
Department of Physics
Advisor: John A. Tanis, Ph.D.

Western Michigan University
Kalamazoo, Michigan
April 2009

ACKNOWLEDGMENTS

First and foremost, I would like to express my deep and sincere gratitude to Prof. John A. Tanis whose tireless and endless supervision, motivation, and encouragement have made my research possible.

It is my pleasure to acknowledge the valuable and constructive suggestions I have received from my doctoral committee members Prof. N. Stolterfhot, Prof. A. Kayani, and Prof. P. Ari-Gur, graduate advisor Prof. Dean Halderson, and department chairman Prof. Paul Pancella.

My special thanks go to all the technical and official staff of the Physics Department for their help during my stay at Western.

I thank all my friends, colleagues, and room mates, particularly, Mr. B.M. Rai, Mr. L. Dumitriu, Ms. I. Dumtriu, Mr. B.S. Dassanayake, Mr. D.P. Cassidy, Mr. J.L. Baran, Ms. A. Ayyad, Mr. A. Aowal, Mr. D. Adams, Miss R.J. Bereczky, Miss A. Simon, Mr. K.P. Dhakal, Mr. A. Dissanayake, and Mr. D.P. Singh, who have been always there throughout the many ups and downs of my journey.

My gratitude to the Department of Physics, Graduate College, Gwen Frostic Doctoral Fellowship, National Science Foundation, and Research Corporation for providing me the financial support not only to conduct the Dissertation work but also for presenting the results of my research at various international conferences.

Last but not the least, my heartfelt thanks to my parents, brother, sister, and

my Guruji for their wholehearted support, help, encouragement, and blessing, without which I would not have even thought of starting this long journey.

Susanta Das

TABLE OF CONTENTS

Table of Contents—continued

CHAPTER

LIST OF TABLES

LIST OF FIGURES

List of Figures—continued

List of Figures—continued

CHAPTER I

INTRODUCTION

The interaction of slow highly charged ions (HCIs) with solid surfaces of metals, insulators, and semiconductors has been the subject of study for nearly two decades [1—36]. These studies primarily involve the influence of the potential energy (PE) stored in HCIs on a solid surface upon impact and neglect the kinetic energy (KE) associated with the HCIs [1, 3]. Fundamental investigations include the study of electron transfer between the approaching projectile and the solid surface [1, 3], production of x-rays [1, 16, 21], neutral and ionized particles [1, 4, 6, 7, 17, 18], electronic excitation of the projectile and surface [1, 5, 16], inelastic scattering of the HCIs [1, 5, 16], Auger processes [1, 15, 20], stopping and neutralization of the projectile [1, 4, 5], formation and decay of hollow atoms (HAs) (an atom with empty inner shells but filled higher shells) above or below the surface [1, 3, 5, 8, 9, 15, 19], and formulation of the classical-over-the-barrier (COB) model [2, 3]. On the other hand, potential applications of HCIs–surface interactions concentrate on surface modifications [23, 24, 29, 32, 34, 35, 36], quantum computers [25, 27], ion beam lithography [28], medicine [13], astrophysics [13], microelectronics [30], and nanotechnology [13, 30], to name a few.

According to the COB model, electrons from the surface are predominantly transferred to an approaching HCI by overcoming the potential well (barrier) between the surface and the HCI classically rather than by quantum mechanical tunneling [2]. In the COB model the 'critical distance' at which the HCIs start capturing electrons from the surface, i.e., the point at which HA formation begins, can be written as

$R_c = \frac{\sqrt{2q}}{W_\Phi}$, where q is the charge state of the incident ions and W_Φ is the work function of the material. Using this model it can also be shown that the principal quantum number n_c corresponding to the highest Rydberg state of the HCI to which the first electron form the surface is transferred is given by $n_c \sim \frac{q}{\sqrt{2W_\Phi\left(1+\sqrt{q/8}\right)}}$ [1, 2, 14].

Particular attention has been paid to the interaction of HCIs with the inner surfaces of micro- and nanocapillaries [6—8, 20]. Yamazaki *et al.* [6, 8] used insulating Al_2O_3 nanocapillaries to study multiple electron transfer between the projectile and the capillaries, i.e., formation of HAs and the production of x-rays, avoiding charge-up effects on the inner surfaces of the capillaries by using an additional beam of thermal electrons produced from a tungsten filament around the target. A nickel (Ni) metallic microcapillary foil was used by Ninomiya *et al.* [7] to extract a stable HA in vacuum. The experimental findings were supported by the most widely accepted COB model [2, 3, 17].

In 2002 Stolterfoht and coworkers [37] first demonstrated experimentally the unprecedented transmission of slow highly charged ions through an insulating polyethylene terephthalate (PET or Mylar) nanocapillary foil without appreciable change in the energy or charge state of the incident ions. Transmission was observed for foil tilt angles (ψ) of several degrees with respect to the incident beam direction. The angular distributions of transmitted ions through the PET foil were compared with a PET foil in which the inner walls of capillaries were coated with silver (Ag), giving results that were entirely different. For the insulating PET foil, transmitted ions were observed up to $\psi = \pm 20^\circ$ with a broad width ($\sim 5^\circ$), whereas for the PET foil

covered with Ag, transmission was observed only near 0^{o} with a narrow width ($\sim 1^{o}$) and low intensity. This finding was surprising since it is well understood experimentally and theoretically that highly charged ions are nearly neutralized upon scattering through angles of few degrees or more at a surface [1], a result that was clearly evident for the PET foil covered with Ag.

The most striking feature for the tilted insulating PET foil was that the observed angular distributions were shifted with respect to $\psi = 0^{o}$ and the centroids of the shifted distributions coincided with the corresponding tilt angles. This result suggested that ions are "guided" along the axis of the nanocapillaries. It was proposed that this guiding was due to a self-organizing charge-up of the inner walls of the nanocapillaries [37], which, after a characteristic charging time, deflects the traversing ions causing them to be guided through the sample along the capillary axis.

This observation of guiding has opened up a new field of study and inspired many experimental and theoretical investigations using various types of nanocapillaries and ions of different energy and charge states [38—82]. Stolterfoht and his group [38—42, 44—47, 51—53, 71, 74, 75, 80] further studied the guiding of slow ($\sim 2 - 10$ keV) positive ions through PET nanocapillaries and its dependence on various parameters such as foil tilt angle, energy and charge state of the incident ions, capillary diameter and density, beam current, and time. For slow H_2 molecular ions (1 keV H_2^+ and H_3^+) [44], remarkably negligible fragmentation occurred during the guiding process, further indicating the strength of the guiding effect. It was observed that magnitude of the guiding strength decreases with increasing projectile energy [41, 42, 47] and foil tilt angle [37, 38, 40]. Furthermore, guiding also depends on the properties of the capillary material, alignment of the capillaries, i.e., parallelism of the capillaries inside the foil, and divergence of the incident beam [39, 48—56]. However,

guiding does not appear to depend on the mass of the incident ions or the background pressure in the scattering chamber [45, 53].

Using the experimental results, Stolterfoht *et al.* proposed a *model* for capillary guiding [38, 40, 53]. According to this model, initially the incident ions are deposited mainly in the entrance region of the capillaries for a certain period of time, hence forming charge patches. The Coulomb field produced by these charge patches then provides an effective trampoline for subsequent incoming ions to guide them through the capillaries. The model, along with the experimental findings, shows that the angular width (full width at half maximum, Γ) of the transmitted ions depends on the energy and charge state of the incident ion beam [46, 53], increasing with the charge state while decreasing with the incident ion energy. These investigators [46, 47, 51, 53] also determined the ability of the capillaries to guide the ions, represented by the *characteristic guiding angle* ψ_c. Two universal scaling laws connecting, respectively, ψ_c and Γ with the energy-to-charge ratio of the projectile [46, 47, 51, 53] were obtained. The experimental results also revealed a linear relation between ψ_c and Γ suggesting that the charge patches in the entrance region are responsible for both the guiding and exit (angular) width of the transmitted ions [51, 53].

In addition to polymer foils, other types of nanocapillaries have been used to study ion guiding such as highly ordered SiO_2 [54] and Al_2O_3 [48, 55, 56, 67] impacted by slow Ne^{q+} (q is the charge state) ions. Theoretical studies of the guiding of slow HCIs through nanocapillaries have been performed by Schiessl *et al.* [57] and Lemell *et al.* [58] using classical trajectory Monte Carlo (CTMC) simulations. Ikeda *et al.* [62, 63] used various glass capillaries to produce micro- and nanometer-sized slow HCIs beams. Guiding of low-energy (200 — 350 eV) electrons through Al_2O_3 with observations similar to positive ions but yielding smaller values of ψ_c than

positive ions has been reported by Milosavljević *et al.* [59]. Recently, Bereczky *et al.* [73] and Dassanayake *et al.* [79] reported transmission of slow HCIs and electrons, respectively, through a single macroscopic glass capillary.

The guiding of highly charged ions and electrons through insulating nanocapillaries has potential applications in the field of micro- and nanotechnology such as the production and focusing of nanometer sized beams for surface modification [23, 24, 30, 32, 60], cell surgery [63, 66], ion beam lithography [28], high-resolution information displays, accelerator-based materials and medical research [30, 63], single ion implantation for nano-hillocks and quantum computers [25—27], and electron microscopy [62]. Guiding also presents a theoretical challenge for the study of the interactions of HCIs and electrons with inner surfaces of the nanocapillaries.

The motivations behind this dissertation research to investigate the guiding of electrons through insulating nanocapillaries are manifold. First, it is of interest to investigate whether electrons are guided through insulating nanocapillaries in a fashion similar to positive ions, and to determine the differences between electron and positive ion guiding. Furthermore, how does electron guiding phenomenon depend on the incident electron energy and the foil tilt angle? Does there exist a universal scaling law similar to that for positive ions? This dissertation focuses on the guiding of medium to high energy electrons through an insulating polyethylene terephthalate (PET) nanocapillary foil.

CHAPTER II

OVERVIEW OF PREVIOUS WORK

In this chapter an overview of experimental and theoretical results for ion and electron guiding reported by various groups using different types of nanocapillaries of varying aspect ratios and densities is presented. It was already mentioned in chapter I that ion guiding depends on parameters such as the energy (E_p) and charge state (q) of the incident ions, foil tilt angle (ψ), capillary aspect ratio (ξ), alignment of capillaries in the foil (Γ_{par} = FWHM of the capillary parallelism), time, capillary density, divergence of the incident beam, and the properties of the capillary material.

In 2002 Stolterfoht *et al.* [37] first reported the guiding of 3 keV Ne^{7+} ions through an insulating polyethylene terephthalate (PET or Mylar) nanocapillary foil of 10 μm length (L) and 100 nm diameter (D) (aspect ratio $\xi = L/D = 100$). The measurements were performed at the 14.5 GHz Electron Cyclotron Resonance (ECR) source at the Hahn-Meitner-Institut (HMI) Berlin, Germany. The nanocapillaries were prepared by chemical etching of the ion tracks created by high energy projectiles (1 GeV xenon ions) incident on the PET foil. Both sides of the sample were subsequently coated with a gold layer of thickness ~ 30 nm, deposited onto the foil at an angle of 45°, to avoid charge-up on the surfaces during ion bombardment. The sample was mounted on a goniometer in an ultra high vacuum (UHV) chamber of background pressure ~ 10^{-10} mbar. The Ne^{7+} ion beam from the ECR source was collimated to a diameter of ~ 1.5 mm and the transmitted ions were analyzed with an electrostatic analyzer of energy resolution 5% and acceptance angle 0.8° (FWHM). The current measured on the sample was ~ 1.3 nA. The observation angles (θ) and foil tilt angles (ψ) both were measured with respect to the incident beam direction.

Ion guiding was observed up to foil tilt angles of $\psi = 20^{\circ} - 25^{\circ}$ without appreciable energy loss or change in the charge state of the incident ions [37, 38]. The guiding was found to decrease strongly with ψ, and the FWHM of the transmitted ions, which was broad ($\Gamma \sim 5^{\circ}$) and larger than the capillary nominal opening ($\Gamma_{aspect} = \frac{L}{2 \times D} \times 57.2^{\circ} = 0.28^{\circ}$), was nearly independent of ψ [37, 38]. From the measured spectra of the transmitted ions at angles $\theta = \psi = 0^{\circ}$ and 5° the intensities of other charge states ($Ne^{0,1,2,3,4,5,6+}$) were observed to be very small (~ 99% of the transmitted ions were Ne^{7+}), suggesting that the incident Ne^{7+} ions underwent negligible charge exchange during passage through the capillaries. This observation verified that ion transmission through insulating capillaries is fundamentally different from that the capillaries of conducting materials [7].

Experimental investigations showed that the guiding ability of the capillaries decreases with decreasing charge state, increasing projectile energy, and increasing foil tilt angle [38, 41, 42, 53]. The FWHM of transmitted ions Γ was always found to be larger than that due to the aspect ratio Γ_{aspect}, and nearly independent of ψ, increasing with increasing charge state, decreasing with increasing incident energy, and likely decreasing with decreasing capillary density [37, 38, 40—42, 50]. It was observed that Γ increased slightly with foil tilt angle at higher incident energies though the variation may not be significant [53]. Recent studies by Stolterfoht *et al.* [74] with 3 keV Ne^{7+} ions guided through PET nanocapillaries of the same length (200 nm) but different densities (1×10^{8} cm^{-2} and 4×10^{6} cm^{-2}) showed that the yield of the transmitted ions for the sample with higher density is greater than for the lower density one. Moreover, the FWHM of $\Gamma = 3^{\circ}$ was found to be independent of ψ for the high density (1×10^{8} cm^{-2}) capillaries, but increased from 2.4° to 4.0° as ψ increased

from 0^{o} to 8^{o} for the low density (4×10^{6} cm^{-2}) capillaries [74]. Furthermore, the value of guiding angle ψ_c was found to be same (5.1^{o}) for both capillaries [74]. This result suggests that the guiding power is mainly governed by the field produced due to the deposition of charge patches near the capillary entrance and neighboring capillaries do not play a significant role in the guiding [74]. It should also be noted that nonparallelism of the capillaries inside the foil plays a minor role in broadening the Γ [39].

In more recent measurements guiding angle was found to be $5^{o} - 6^{o}$ using the capillaries of diameters of 100, 200, 300, and 400 nm suggesting that guiding does not depend appreciably on the capillary aspect ratio [71], in contrast to the earlier findings in which guiding efficiency of capillaries was found to increase with capillary aspect ratio [45].

The time evolution of ion guiding (characteristic charging time) showed that Γ increases during the charging process from a value close to the capillary aspect ratio at the beginning when $Q = 0$ (i.e., no charge deposition, where Q is the deposited charge) to its final value (larger than Γ_{aspect}) for all values of ψ once the equilibrium condition $Q = Q_{\infty}$ (i.e., the final deposited charge on the inner surfaces of the capillaries) is achieved [39, 52]. This result suggests that the broadening of the angular width is due to the charge deposition near the entrance of capillaries.

Recent measurements of the time evolution of the transmission profiles of ions in PET nanocapillaries showed that the profiles exhibit three localized peaks with the central one corresponding to the foil tilt angle ψ [75]. These peaks change in intensity significantly with time, i.e., with deposited charge, producing an oscillatory movement of the mean emission angle ($\alpha = \theta - \psi$) during the charge-up process of the capillaries. As the charge-up progresses towards equilibrium, the oscillation is

damped, the central peak dominates, the mean emission angle coincides with ψ, and no longer changes with time. This oscillatory behavior has been attributed to the formation of temporary charge patches inside the capillary in addition to the primary charge patch. These temporary charge patches are important in the pre-equilibrium period but do not play any significant role in the guiding process once the equilibrium condition is achieved [49, 52, 57, 58, 75].

Based on the experimental results, a model for capillary guiding was proposed in which the capillary is divided into two regions: *scattering* and *guiding* [37, 38, 40, 51—53]. In the scattering region incident ions retain their memory of the incident foil tilt angle and are scattered by the Coulomb field of already deposited ions. After several subsequent scatterings they lose their memory of the incident angle and enter into the guiding region where they are transmitted along the axis to the capillary exit with a FWHM Γ that is independent of ψ. Using the fact that most of the charges are deposited in the entrance region, known as the *entrance patch* (Q_∞), during the charge-up process [57], it was suggested that these entrance patches produce *deflection* or *scattering* (U_s) and *broadening* or *guiding* (U_g) *potentials* in the entrance and exit regions of the capillary, respectively [38, 40—42], and their relative strengths could be determined using the fact that both depend on Q_∞, E_p, and q [53].

It should be mentioned that the time dependent *charging* and *discharging* processes of capillaries were also considered in the model calculation [37—42, 46, 52, 53]. Here, charging refers to the time during which the charge deposition takes place at the entrance region of the capillary in order to establish the ion guiding. This time is known as the *characteristic charging time* τ_c [38, 40, 41, 52]. The *discharging time* τ_d is attributed to the surface and bulk conductivities of the capillary due to deposited charges [38, 40, 41, 52].

The experimental results [52, 53] show that at equilibrium the fraction $f(\psi)$ of transmitted ions decreases with the energy (E_p) of the incident ions and tilt angle ψ. These observations, in conjunction with model calculations, reveal that $f(\psi)$ is primarily influenced by the U_s and can be expressed as $f(\psi) = f(0)\exp\left(-\frac{E_p}{qU_s}\sin^2\psi\right)$, where $f(0) \leq 1$ is the transmitted ion intensity at $\psi = 0^\circ$. Furthermore, Γ has been found to depend on U_g, E_p, and final charge state q_f of the transmitted ions and can be written as $\Gamma = 2\sqrt{\ln 2 \frac{q_f U_g}{E_p}}$ [40, 41, 44, 51, 52], which matches very closely the experimental values. Using the equation for Γ it was found that the potential (U_g) necessary to guide the 3 keV Ne^{7+} ions is ~ 1.0 V, which is very close to the calculated value of ~ 0.8 V [37]. Significantly, it was observed that the intensity and width (Γ) of the transmission profiles (angular distributions) through PET capillaries are nearly equal for 7 keV Ne^{7+}, 13 keV Ar^{13+}, and 25 keV Xe^{25+} ions, i.e., for constant energy-to-charge ratio, suggesting that the major parameter influencing the guiding is the energy to charge ratio, which, in turn, indicates that guiding does not depend on the mass of the incident ions [53].

The ability of the capillaries to guide the ions is known as the *characteristic guiding angle* ψ_c, defined as the angle at which transmitted intensity falls to $\frac{1}{e}$ of its value at $\psi = 0^\circ$, i.e., $\frac{f(\psi_c)}{f(0)} = \frac{1}{e}$ [46]. It has been observed that ψ_c depends on the charge deposition in the entrance region, properties and surface treatment of capillaries, and capillary density [46, 51–53]. The experimental results led to two *universal scaling laws* respectively, (1) $\sin^{-2}\psi_c = \frac{E_p}{qU_s}$, and (2) $\sin^{-2}\Gamma = \frac{1}{4\ln 2}\frac{E_p}{qU_g}$,

which in turn, give a linear relationship between ψ_c and Γ and of the form $\psi_c \approx 1.8\,\Gamma$ for Ne^{7+}, Ar^{13+}, and Xe^{25+} ions for the PET capillaries, further suggesting that the entrance charge patches produce both U_s and U_g [46, 51, 53].

Schiessl *et al.* [57] performed calculations using the classical trajectory Monte Carlo (CTMC) model to simulate guiding by highly charged ions through nanocapillaries. The results showed that most of the charges are deposited in the entrance region during the charge up process and that the angular width (Γ) of the transmitted ions should have a value close to the capillary aspect ratio. However, Skog *et al.* [68] reported that charge patches are formed sequentially and distributed along the whole length of the capillaries during the charging-up process. These patches are maintained even after the equilibrium condition is reached and play a significant role in the process of guiding, in contrast to the earlier results reported by Stolterfoht *et al.* [39, 52, 53] and Schiessl *et al.* [57] in which only the charge patches formed in the entrance region of the capillaries play a significant role in guiding.

Kanai *et al.* [49] measured the two-dimensional (2-D) images of 3.5 — 7 keV Ne^{7+} ions transmitted through PET nanocapillaries (density = 4×10^6 cm^{-2}, length 10 μm, and diameter 200 nm) during the charging process, i.e., the intensity evolution of the transmitted ions, using a 2-D position sensitive detector (PSD). It was observed that the 2-D images oscillate in position and change shape from circular at the beginning to oval as the charging process proceeds. However, once saturation (equilibrium) was reached the 2-D images became stable, with a circular width $\Gamma \sim 1^\circ$ as predicted by Schiessl *et al.* [57]. Also, Γ for 7 keV ions was smaller than for 3.5 keV ions, showing that Γ decreases with increasing projectile energy, in accordance with the results obtained by Stolterfoht *et al.* [40—42]. Fürsatz *et al.* [50] and Stolterfoht *et al.* [52] also reported observations similar to Kanai *et al.* [49].

Víkor *et al.* [43] investigated the guiding of 7 keV Ne^{7+} ions through PET capillaries of length 10 μm and diameter 100 nm (aspect ratio 100) and observed guiding up to $\psi = 4^{\circ}$. It was found that $\Gamma \sim 3.2^{\circ}$ which is smaller than the $\Gamma \sim 5^{\circ}$ obtained by Stolterfoht *et al.* [37] using 3 keV Ne^{7+} ions through PET capillaries of the same aspect ratio, again showing that Γ decreases with increasing incident ion energy. The magnitude of the guiding potential was also calculated using the model given by Stolterfoht *et al.* [40, 41], giving a value $U_g \sim 0.5$ V.

Mátéfi-Tempfli *et al.* [48] prepared Al_2O_3 nanocapillaries of length 15 μm and diameter 280 nm and found ion guiding up to $\psi = 7.5^{\circ}$ for 3 keV Ne^{6+} ions. The observed Γ was broad ($\sim 5.5^{0}$) and very close to the value ($\sim 5^{\circ}$) found by Stolterfoht *et al.* [37] for PET capillaries of length 10 μm, diameter 100 nm, and the same incident energy for Ne^{7+}. It was also observed in Ref. [48] that the characteristic guiding angle ψ_c of the capillaries [48] was smaller than for 200 nm diameter capillaries and Ne^{7+} ions, showing that guiding decreases with increasing capillary diameter and decreasing charge state [37, 45, 52, 53].

In other studies, Sahana *et al.* [54] reported guiding of 7 keV $Ne^{6,7+}$ ions through highly ordered SiO_2 nanocapillary arrays of length 25 μm, diameter ~ 100 nm, and density ~ 10^8 cm^{-2}. Guiding was observed only up to $\psi = 4^{\circ}$ and Γ was found to have a value close to the capillary aspect ratio ($\sim 1^{\circ}$) predicted by Schiessl *et al.* [57]. However, the Γ for Ne^{6+} ions was broader than for Ne^{7+} ions, in contrast to the results and model proposed by Stolterfoht *et al.* [37, 40, 41, 44, 51]. Skog *et al.* [55] reported the guiding of 7 keV Ne^{7+} ions through Al_2O_3 capillaries of length 10 μm and diameter ~ 60 nm ($\xi \sim 160$), density $\approx 10^8$ mm^{-2}, $\Gamma_{par} \sim 0.5^{\circ}$, and $\Gamma_{aspect} \sim 0.34^{\circ}$ for tilt angles up to $\psi = 4^{\circ}$. The measured $\Gamma \sim 1^{\circ}$ was close to the capillary aspect ratio. On the other hand, ψ_c was found to have the value ~ 1.1°, smaller than the values

measured for SiO_2 (2.8°) and PET (2.7°) [46, 51, 53] capillaries. Krause *et al.* [56] used 200 MeV Ti^{+12} ions to determine the alignment of Al_2O_3 capillaries of length 60 μm and diameter 100 nm (ξ = 600) inside the foil, and then studied the guiding of slow Ar and Ne ions of different charge states. Guiding was observed only up to 0.5° with much lower transmitted intensities compared to PET.

Milosavljević *et al.* [59] reported the guiding of electrons with energies 200 — 350 eV through Al_2O_3 of length 15 μm and diameter 140 nm (aspect ratio = 110) with observations similar to positive ions but found that electron guiding falls faster than for positive ions. Additionally, the guided electrons were found to be transmitted with negligible energy loss. Transmission of 2 — 120 eV electrons through an Al_2O_3 nanocapillary foil of same aspect ratio was also reported by the same authors [82].

Xi-Meng *et al.* [69] studied the guiding of 60 keV O^{6+} ions through uncoated Al_2O_3 nanocapillaries of length 10 μm and diameter 100 nm (Γ_{aspect} = 0.57°) and found that ψ_c (2.16°) is larger than for gold-coated capillaries (1.1°) [55], suggesting that a larger equilibrium charge is required to guide the ions in the uncoated sample. These authors [72] further investigated the guiding of 60 and 120 keV O^{3+} ions through Al_2O_3 nanocapillaries of length 10 μm and diameter 50 nm (ξ = 200) and found results similar to Stolterfoht *et al.* [37, 38, 40, 42]. Li *et al.* [77] compared ion transmission for both front- and back-surface coated and only front-surface coated polycarbonate foils. The transmission of ions through only front-coated nanocapillary foils, and the corresponding ψ_c, was found to be smaller than for foils with both surfaces coated, suggesting an influence of the charged back side on the transmission properties.

For considerably larger diameter capillaries, Bereczky *et al.* [73] reported the guiding of 4.5 keV Ar^{9+} ions up to $\psi \sim 5°$ through a single straight glass

macrocapillary of length 11.4 mm and diameter 170 μm, while Dassanayake *et al.* [79] reported the guiding of 500 eV electrons through a similar single glass capillary. Quantitative studies of the characteristics of ion and electron transmission through these macrocapillaries, as well as the similarities and differences with nanocapillary foils, are ongoing.

CHAPTER III

GUIDING MECHANISM

It was noted in Chapter I that the *guiding* of slow highly charged 3 keV Ne^{7+} ions through an insulating PET nanocapillary foil of aspect ratio 100 was first demonstrated experimentally by Stolterfoht *et al.* [37], stimulating many new investigations [38—82]. Many of the experimental results have been modeled by Stolterfoht and his group [37—42, 44—47, 51—53], while Schiessl *et al.* [57] have performed theoretical simulations to help understand the observations. Recently the guiding of slow electrons with observations similar to positive ions has been reported [59].

A schematic of capillary guiding is shown in Figure 1, in which the tilt angle ψ of the foil and the observation angle θ are both measured with respect to the incident beam direction, and $\alpha = \theta - \psi$ is the emission angle of transmitted ions measured with respect to the capillary axis. Both sides of the capillary foil are coated with a thin metallic film to prevent the incident ions from building up charge on the surfaces. Initially, incident ions are deposited on the inner surfaces of the insulating capillaries in a self-organizing manner due to the charging up of the insulating walls. Monte-Carlo simulations [57] have shown that most of the incoming ions are deposited in the entrance region of the capillaries and therefore form charge patches in that region. Hence, this entrance region has been called the *patch region.* Additional charge patches (secondary and tertiary) can also be formed deeper inside the capillaries after the entrance patches are formed but their contribution to ion guiding is less important [57].

The ion deposition takes place for a certain period of time, known as the *characteristic charging time* with *time constant* (τ_c), and produces an electric field inside the capillaries. Under equilibrium conditions this electric field provides an effective "trampoline" for subsequent incoming ions, causing them to be guided along the capillary axis to the capillary exit. In this case the ions are scattered at distances greater than the critical distance $R_c = \frac{\sqrt{2q}}{W_\Phi}$, where q is the charge state of the incident ions and W_Φ is the work function of the material, inhibiting electron capture by the incident ions from the capillary walls [1, 3, 57, 58].

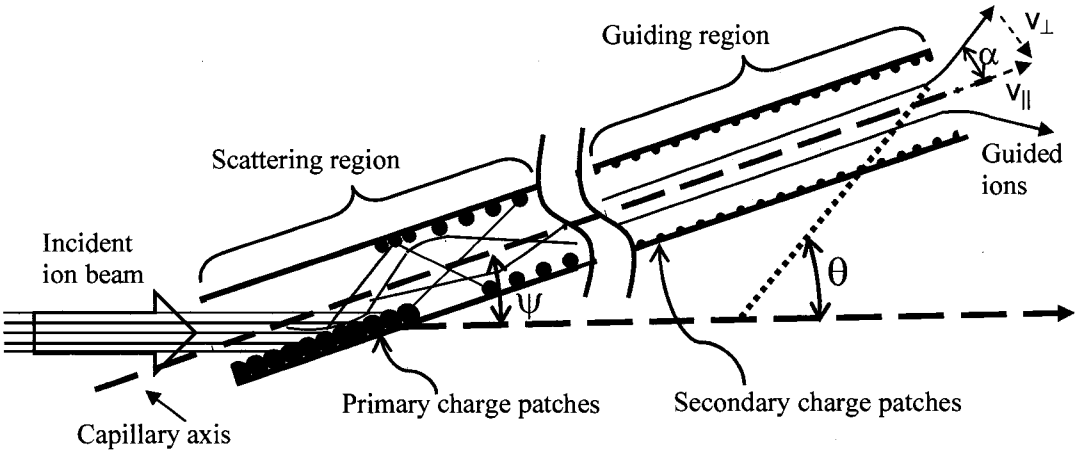

Figure 1. Guiding of ions in an insulating nanocapillary.

It has been found that the angular widths, i.e., full width at half maximum (FWHM) Γ, of the transmitted ions are nearly constant and independent of the foil tilt angle ψ [37, 38, 40, 53]. To understand these observations, the capillary is divided into two regions: *scattering* and *guiding* [37, 38, 40, 52, 53]. These regions are considered to be independent, i.e., processes occurring in the scattering region do not affect those in the guiding region. In the first region incident ions are scattered by the already deposited ions (entrance patches) from one side of the wall towards the other

side and retain memory of the incident angle direction. After several scatterings they completely lose their memory of the incident angle and enter the guiding region where they are directed along the axis and exit the capillary with a FWHM independent of ψ. As most of the charges are deposited in the entrance region [57], it is believed that the entrance patches are mainly responsible for the scattering and guiding of the ions. Thus, the propagation of ions through the scattering and guiding regions is characterized by the tilt angle ψ, and the divergence angle α, respectively.

The entrance charge patches produce a quasi linear potential of depth U_s, known as *deflection potential*, across the diameter of the capillary which is responsible for the angular scattering (angular straggling) of the ions from one side of the capillary wall to the other side [38, 40, 41, 53]. Moreover, these charge patches produce a symmetric potential of depth U_g, called the *broadening potential*, at the capillary exit [38, 40, 41, 53]. Hence, at the exit the ions are defocused which, in turn, leads to broadening of the transmission profile. In the guiding region, because of U_g the ions may gain a transverse kinetic energy $E_\perp = q_f U_g$, and a corresponding velocity $v_\perp$. The emission angle α of transmitted ions relative to the capillary axis, which is very small, then can be obtained from $\sin\alpha \approx \alpha = \frac{v_\perp}{v_\parallel} = \sqrt{\frac{q_f U_g}{E_p}}$, where q_f, E_p and $v_\parallel$ are the final charge state of the transmitted ions, the projectile energy, and the longitudinal (incident) projectile velocity, respectively. Therefore the transverse kinetic energy is related to the projectile kinetic energy as $E_\perp = E_p \sin^2\alpha$. The ions are deflected (guided) if the transverse kinetic energy $E_\perp = \frac{v_\perp^2}{2}$ does not exceed the value of $q_f U_g$ [38, 40, 53]; otherwise they strike the wall.

The FWHM of the angular distributions of transmitted ions is related to U_g and the incident ion energy E_p and can be modeled as [38, 40, 41, 51, 53]

$$\Gamma = 2\sqrt{\ln 2 \frac{q_f U_g}{E_p}}. \qquad 1$$

Equation 1 shows that for a constant potential of depth U_g the angular width is proportional to $\sqrt{\frac{q_f}{E_p}}$, thereby increasing with charge state and decreasing with projectile energy for a fixed foil tilt angle ψ. Experimentally, it was observed that Γ matches very closely with the value given by Equation 1 [38, 40, 41, 51, 53].

Experimental observations show that guiding depends strongly on the projectile energy [41, 42, 53], foil tilt angle [40, 41, 42, 53], and the material properties [46, 48, 53]. As noted earlier, guiding decreases with increasing incident projectile energy and foil tilt angle, but increases with charge state [40, 42, 46, 47, 53]. Also, increase in the incident current density does not significantly affect the capillary guiding [52]. It should be pointed out that ion guiding apparently does not depend on the mass of the ion [53].

Since most of the charges are deposited in the entrance region, the time evolution of charge (Q) deposition can be written as [38, 40, 41, 52]

$$\frac{dQ(t)}{dt} = j_{in} - j_d(Q) - j_{tr}(Q), \qquad 2$$

where j_{in} is the incident current entering the capillary, $j_d = dj_{in}$ is the discharge current due to the surface and bulk conductivities of the capillary, and $j_{tr} = fj_{in}$ is the current transmitted through the capillary. Here d represents the fraction of the incident current that flows to ground through the capillary wall, while f represents the fraction of the incident current transmitted through the capillary. The charge deposition

reaches its equilibrium value Q_∞ with characteristic charging time τ_c, and Equation 2 can be written as [52]

$$\frac{dQ}{dt} = 0 = j_{in} - j_d(Q_\infty) - j_{tr}(Q_\infty). \qquad 3$$

Since Q_∞ does not change appreciably with j_{in} at equilibrium, j_d must increase strongly with deposited charge. It should also be noted that the transmitted intensity decreases strongly with increasing foil tilt angle ψ suggesting significant charge depletion in the entrance region, which can be attributed to the sudden increase of the discharge current, i.e., an increase in the surface and bulk conductivities of the capillary [38, 40, 41, 52]. It was observed that discharging of the capillary through surface conductivity is higher than through the bulk [52]. This increase in discharge current is known as a Frenkel-Poole process [52] and can be written as $j_d(Q) = \frac{Q}{\tau_d} e^{\sqrt{\frac{Q}{Q_d}}}$, where Q_d and τ_d are, respectively, the characteristic charge and time constants for capillary discharge [38, 40, 41, 46, 51, 52].

It is observed that the fraction f of transmitted ions depends exponentially on E_p and ψ which can be modeled under equilibrium conditions from experimental findings as [38, 40, 41, 52, 53]

$$f(\psi) = f(0)\exp\left(-\frac{E_p}{qU_s}\sin^2\psi\right), \qquad 4$$

where $f(0) \le 1$ is the transmitted fraction at ψ = 0°, q is the initial charge state of the incident ions, and $U_s\left(=\frac{Q}{C_s}\right)$ is an average potential across the capillary diameter produced by the charge deposition in the entrance region, Q is the total charge deposited on the capillary wall, and C_s is the capillary capacitance. Because the

charge patches in the entrance region are dominant, both U_s and U_g are attributed to these charge patches [38, 40, 53]. The potential U_s, known as the *deflection potential*, is responsible for the intensity of the transmitted ions, whereas the *broadening potential* U_g in the exit region plays the crucial role in broadening the transmission profiles [41, 53].

Equation 4 shows that $f(\psi)$ decreases exponentially with the square of the sine of the tilt angle ψ and the experimental results can be well fitted by the Gaussian-like function [46, 51, 52, 53]

$$f(\psi) = f(0)\exp\left(-\frac{\sin^2\psi}{\sin^2\psi_c}\right), \qquad 5$$

where ψ_c is the characteristic *guiding angle*. It should be noted that ψ_c represents the angle at which the transmitted intensity falls to $\frac{1}{e}$ of its value at ψ = 0°, i.e., $\frac{f(\psi_c)}{f(0)} = \frac{1}{e}$ [46, 47].

Since Equations 4 and 5 are of the same form, we deduce that [46, 53]

$$\sin^{-2}\psi_c = \frac{E_p}{qU_s}, \qquad 6$$

giving a scaling law for ψ vs. $\frac{E_p}{q}$. Indeed, for constant potential U_s, a nearly linear relationship between $\sin^{-2}\psi_c$ and the projectile energy-to-charge ratio $\left(\frac{E_p}{q}\right)$ was found experimentally [46, 53]. A similar nearly linear relationship between $\sin^{-2}\Gamma$ and $\frac{E_p}{q}$ (second universal scaling law) was also deduced from the experimental observations [53].

Since both Γ and ψ_c depend on $\frac{E_p}{q}$, a relationship between the exit width Γ and the guiding power ψ_c can be expected for capillaries of different aspect ratios. In fact, such a relationship was found for PET capillaries using the data in Table 1.

Table 1: Γ and ψ_c values of PET capillaries with different aspect ratios and densities.

Aspect Ratio (Diameter)	PET sample density (capillaries/cm^2)	Ion beam	Γ	ψ_c	Reference
100 (100 nm)	10^8	3 keV Ne^{7+}	5°	9°	37, 53
50 (200 nm)	4×10^6 and 10^8	3 keV Ne^{7+}	3°	5.4°	46, 51, 53
60 (200 nm)	4×10^6	3.5 keV Ne^{7+}	1.3°	3°	52, 53

These results suggest that although Γ and ψ_c may vary significantly there exists a linear relationship

$$\psi_c = 1.8\,\Gamma \qquad 7$$

for PET capillaries [46, 51, 53]. Equation 7 further verifies that the entrance patches produce both the U_s, required for the guiding, and the U_g, responsible for the angular width of the transmitted ions. However, it was found that the FWHM Γ increases slightly with foil tilt angle ψ at higher incident ion energies though the variation of Γ was within the experimental uncertainties [53]. Also, it was found that both the deflection (U_s) and broadening (U_g) potentials decrease slightly with increasing energy-to-charge ratio, and the potential U_s in the entrance region is nearly an order of

magnitude larger than the potential U_g in the exit region, indicating that both potentials are produced by the same charge patches in the entrance region [53].

The CTMC simulations of Schiessl *et al.* [57] indicate that Γ for the transmitted ions should be ~ 1°, a value close to that found for SiO_2 [54] and Al_2O_3 [55] capillaries. On the other hand, results obtained by Stolterfoht *et al.* [40, 51, 53] show Γ to be as large as 5°. These discrepancies between experimental results and theoretical calculations suggest that other factors such as the properties of the material (dielectric constant, conductivity, etc.), surface treatment, and capillary density also play roles in determining the FWHM [40, 41, 51, 53, 54]. It should also be pointed out that the measurements at the HMI (Berlin) and at RIKEN (Japan) were not able to explain that whether Q_∞ depends on ψ and the incident ion current, and whether the fraction of transmitted ions on depends on the incident ion current [52].

Recently, Skog *et al.* [68] reported that charge patches are formed sequentially and distributed along the entire length of the capillaries during the charging-up process. These patches are maintained even after equilibrium condition is reached and play an important role in the process of ion guiding, in contrast to the earlier results reported by Stolterfoht *et al.* [39, 52], Schiessl *et al.* [57], and Lemell *et al.* [58] in which only the charge patches formed in the entrance region of the capillaries played a significant role in guiding. Moreover, Krause *et al.* [56] reported single, double, and triple collisions of Ar^{q+} and Ne^{q+} ions (q is the charge state of the incident ions) while traversing high porosity (≈ 40 %) relatively thick (length 100 nm and diameter 60 μm) Al_2O_3 capillaries without appreciable loss in the energy or change in the charge state of the incident ions. This latter result is again in sharp contrast to the earlier results for low porosity (1 — 10 %) and thinner (length ~ 10 μm) capillary foils [37—55, 57], in which multiple collisions were not observed suggesting a different

transmission process for long pores. In addition, Monte Carlo simulations [65] of electrons interacting with an amorphous surface of Al_2O_3 at grazing incidence show evidence for inelastic scattering in contrast to results for the scattering of highly-charged ions on a surface, suggesting that electron and ion guiding might be qualitatively and quantitatively different processes.

As noted above, until now most of the model calculations were performed by Stolterfoht *et al.* for positive ions traversing PET samples. Therefore, the validity of Equations 6 and 7 is yet to be confirmed for ions as well as electron guiding through other types of capillaries (SiO_2, Al_2O_3). Also, the influences of incident ion current, capillary density, neighboring capillaries, and material properties have not been fully explored. Therefore, ion and electron guiding remains an open question from both experimental and theoretical viewpoints.

CHAPTER IV

EXPERIMENTAL PROCEDURE

In this chapter the experimental procedure is described. The measurements were performed at Western Michigan University. The main components of the experimental set-up are: (1) an electron gun for generating electrons of the required energy for the experiment, (2) a goniometer for precise positioning of the sample, (3) a 45° parallel-plate electron energy analyzer coupled with a channel electron multiplier (CEM) for detection and counting of electrons transmitted through the sample, and (4) electronics for signal processing and for spectrometer control and data acquisition (DAQ). A PC-based LabView program was used to control and communicate with the electronics, and to acquire the data [83].

A schematic arrangement of the electron gun, collimator, goniometer, and spectrometer coupled with the CEM inside the experimental chamber is shown in Figure 2. The base pressure in the chamber was kept at ~ 10^{-6} Torr by a diffusion pump backed by a mechanical rotary pump. A μ-metal shield was used to minimize stray magnetic fields inside the chamber. Each of the main experimental components are described below.

Electron Gun and Goniometer

A biased tungsten filament inside the electron gun assembly acted as the source of the electron beam. The beam was focused, steered vertically and horizontally, and collimated to a diameter of about 1.5 mm prior to striking the sample. The electron gun and the collimator assemblies used in this experiment are shown in Figures 3 and 4, respectively.

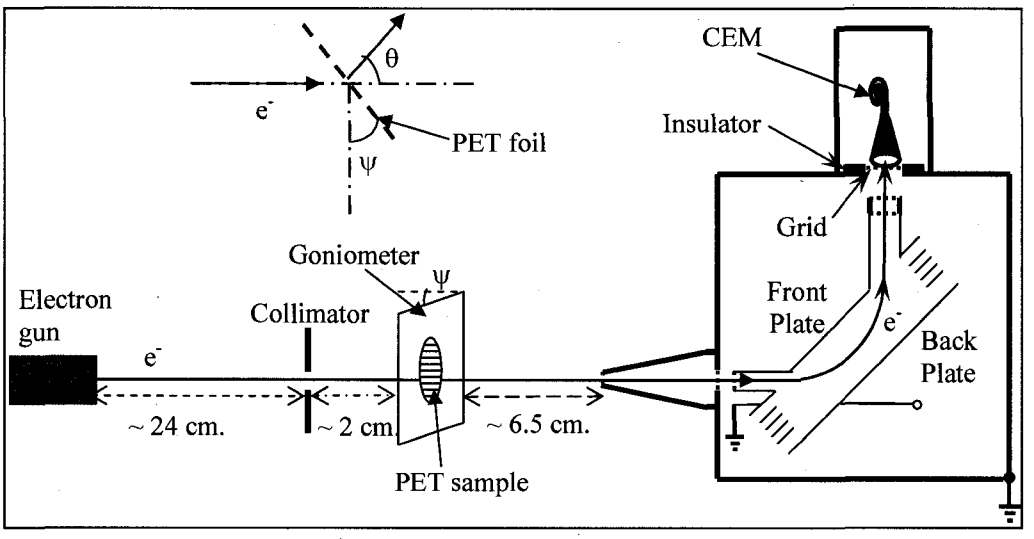

Figure 2. Schematic arrangement of the electron gun, goniometer, spectrometer, and CEM inside the experimental chamber. The capillary tilt angle ψ and observation angle θ are indicated.

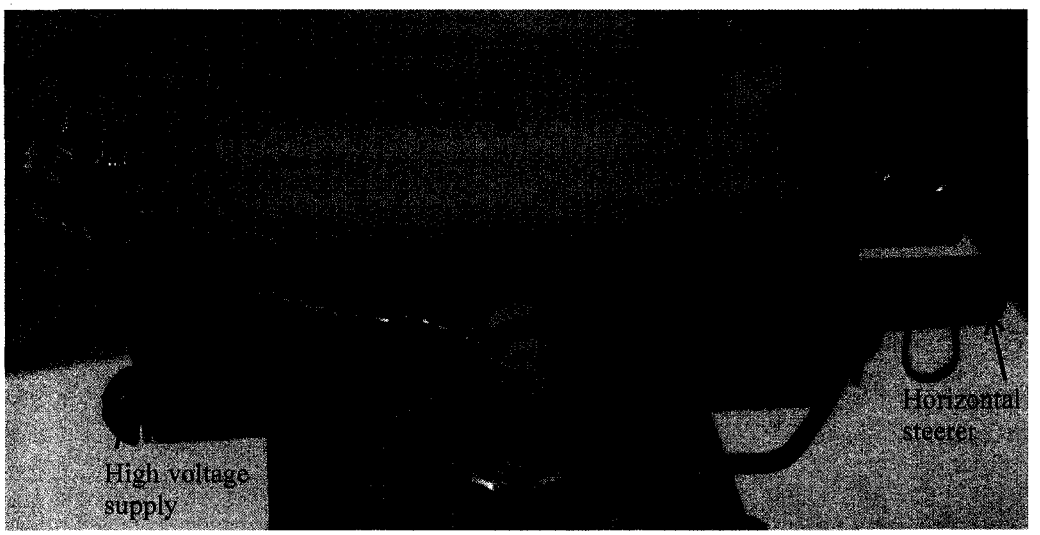

Figure 3. Electron gun assembly. Electrons are produced at the left end from a tungsten filament and exit the right end between the steering plates.

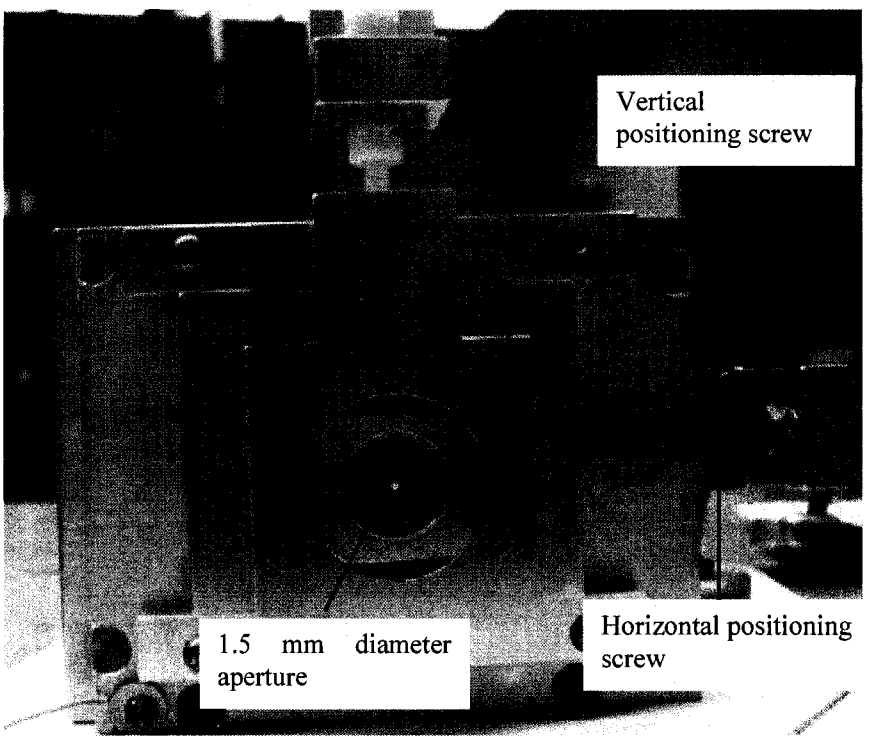

Figure 4. Collimator assembly for the electron beam.

The sample was mounted on the goniometer to allow precise two-dimensional (2-D) positioning of the sample: tilt angle rotation (ψ) about a vertical (V) axis and azimuthal rotation (φ) about a horizontal (H) axis. The tilt angle allows rotation of the sample from -20^{o} to $+20^{o}$, whereas the azimuthal angle allows full rotation from 0^{o} to 360^{o} as shown in Figure 5. The goniometer is controlled by LabView software, for which the control panel is shown in Figure 6.

Spectrometer and Channel Electron Multiplier (CEM)

A schematic diagram of the electron spectrometer is shown in Figure 7 along with the CEM. The spectrometer can be operated in different modes depending on the desired energy resolution and the electron energy range to be investigated [83].

For the present measurements the low-resolution high-energy mode of the spectrometer was used. The entire spectrometer can be rotated (observation angle, θ)

precisely from – 30° to + 30°. The spectrometer [84] consists of a 45° plane-mirror analyzer (PMA) with parallel plates that act as a capacitor and deflect electrons with a given energy (E) through 90° into the CEM. The energy of the transmitted electrons is proportional to the voltage (V) between the two plates, and only electrons in a small energy range make it through the spectrometer and into the CEM.

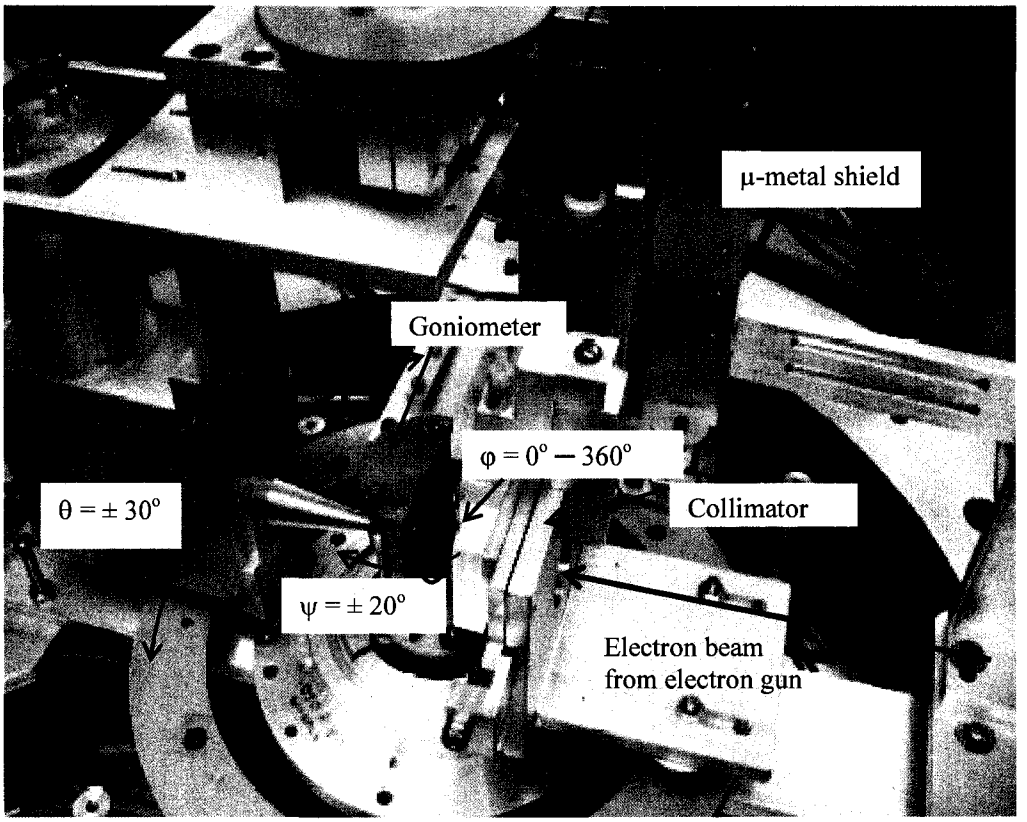

Figure 5. Goniometer inside the chamber with spectrometer, CEM, and collimator.

The energy of the transmitted electrons E is given by

$$E = \frac{eV}{k} \qquad 8$$

where k is a constant determined from the geometry of the spectrometer. The value of k is determined from $k = \frac{Z}{2l}$, where Z is the distance between the entrance and exit

slits of the spectrometer and l is the plate separation [84] as shown in Figure 7. The value of k in this case is 0.60. The energy resolution R of the spectrometer can then be written as $R = \frac{\Delta E}{E} = \frac{2S}{Z}$, where ΔE is the energy spread (FWHM) of the transmitted electrons, and S is the width of the entrance and exit slits (assumed equal). The energy resolution of the spectrometer used in this experiment is 3%.

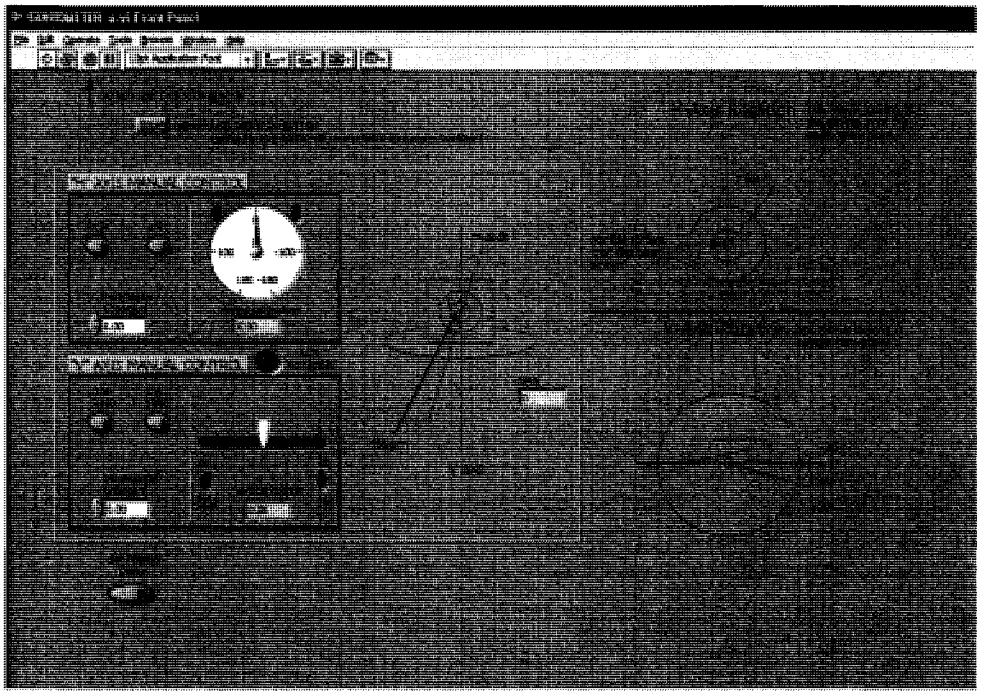

Figure 6. LabView control panel of the goniometer.

The required voltage (in volts) that must be supplied to the spectrometer back plate can then be written from Equation 8 as

$$V = -kE \text{ (eV)} \qquad 9$$

This voltage V deflects the entering electrons by 90°. The voltage V_G on the grid, which blocks low energy electrons, is the same as the back plate voltage of the spectrometer.

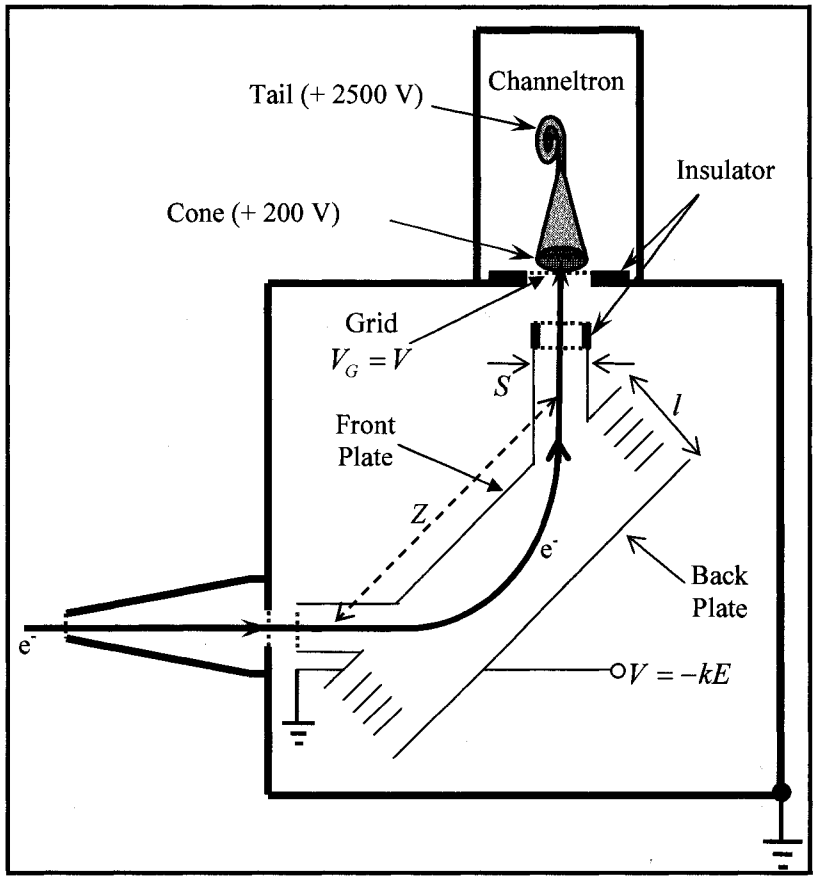

Figure 7. Schematic diagram of the spectrometer and CEM.

An energy spectrum of the transmitted electrons can be obtained by incrementing the voltage on the spectrometer plates over the desired range, and then counting the number of pulses originating from electrons striking the CEM for each plate voltage. A CEM [84, 85] model 4821G with a gain of 1.0×10^8 was used for the present measurements. The CEM was used in the pulse generating mode. The detection efficiency of the CEM depends on the energy of the electrons that enter the CEM. The cone, for initial acceleration of the electrons, and tail of the CEM were biased to + 200 V and + 2500 V, respectively, for optimum detection efficiency. The number of CEM pulses for each plate voltage setting were normalized to the beam

current measured on the sample (goniometer). A LabView data acquisition program was interfaced to a CAMAC Crate that was used [83] to control apply voltage to the spectrometer plates and to control the angular position of the spectrometer to acquire the normalized spectra which were then collected with a PC.

Electronics for Spectrometer Control and Data Acquisition

In order to control the angular positions of the spectrometer precisely and to acquire the electron spectra normalized to the electron beam current measured on the sample, various electronics were used: (a) a Bi Ra Systems 6700-SCB Power Computer Automated Measurement and Control (CAMAC) Crate system was used to host the DAQ equipment, (b) a Highland Technology M210 CAMAC Serial Crate Controller for data exchange between the PC and instruments in the CAMAC Crate, (c) a LeCroy 2415 High Voltage Power Supply to supply the necessary voltage to the spectrometer plates, (d) a LeCroy 2551 Scaler to count the electrons detected by the CEM (Channel 0), and to count pulses proportional to the beam current measured on the sample for the normalization (Channel 2), (e) a Joerger SMC-R Stepping Motor Controller and a Joerger CS-5 Optically Isolated Input Register to precisely control the angular position of the spectrometer, (f) a Keithley 617 Programmable Electrometer to measure the current on the sample (the output of the electrometer was converted into digital pulses and counted by channel 2 of the Scaler as discussed below), (g) a Keithley 197A Autoranging Microvolt Digital Multimeter (DMM) to monitor the voltage of the LeCroy high voltage power supply for the spectrometer, and (h) a Kinetic System 3388 GPIB Interface to monitor and control the General Purpose Interface Bus (GPIB) instruments, i.e., the DMM and the Keithley electrometer through the same CAMAC crate controller. The same LabView program

mentioned above was used [83] to communicate with these instruments and to acquire the data.

A block diagram of the electronics is shown in Figure 8. Transmitted electrons from the sample were analyzed by the spectrometer and counted by the CEM. Signals from the CEM of height ~ 10 mV were amplified by 200 times (2 V) by a fast linear amplifier and input to a constant fraction discriminator (CFD). The threshold level of the CFD was set to about 0.5 V to remove electronic noise. The NIM logic output (−1V) signal of the CFD was then sent to channel 0 of the LeCroy Scaler to be recorded by the PC. These counts were normalized to the electron beam current measured on the sample using a Keithley electrometer. The current read by the electrometer produces a 0 — 2 V dc output proportional to the input current. The voltage output of the electrometer was dropped across a 1 MΩ resistor to convert the output voltage to a current. The current was then converted into TTL digital pulses (~ +5 V) by a Digital Current Integrator (DCI), and, in turn, were input to a Gate and Delay Generator to convert them into NIM logic pulses. These pulses were then counted by channel 2 of the LeCroy scaler. In this way, transmitted electrons of different energies, ranging from an initial value to an ending value, were counted, hence completing one full scan of the electron energy spectrum. The LabView program allows acquiring multiple scans of the transmitted electron energy spectrum over the specified energy range for better statistics. It is noted that although there are three LeCroy high voltage power supplies and three DMMs in the CAMAC Crate system, only one high voltage power supply and one DMM was used for the current measurements, since only one spectrometer was used for analyzing the transmitted electrons as shown in Figure 8. The user control panel for the spectrometer and the data acquisition are shown in Figure 9.

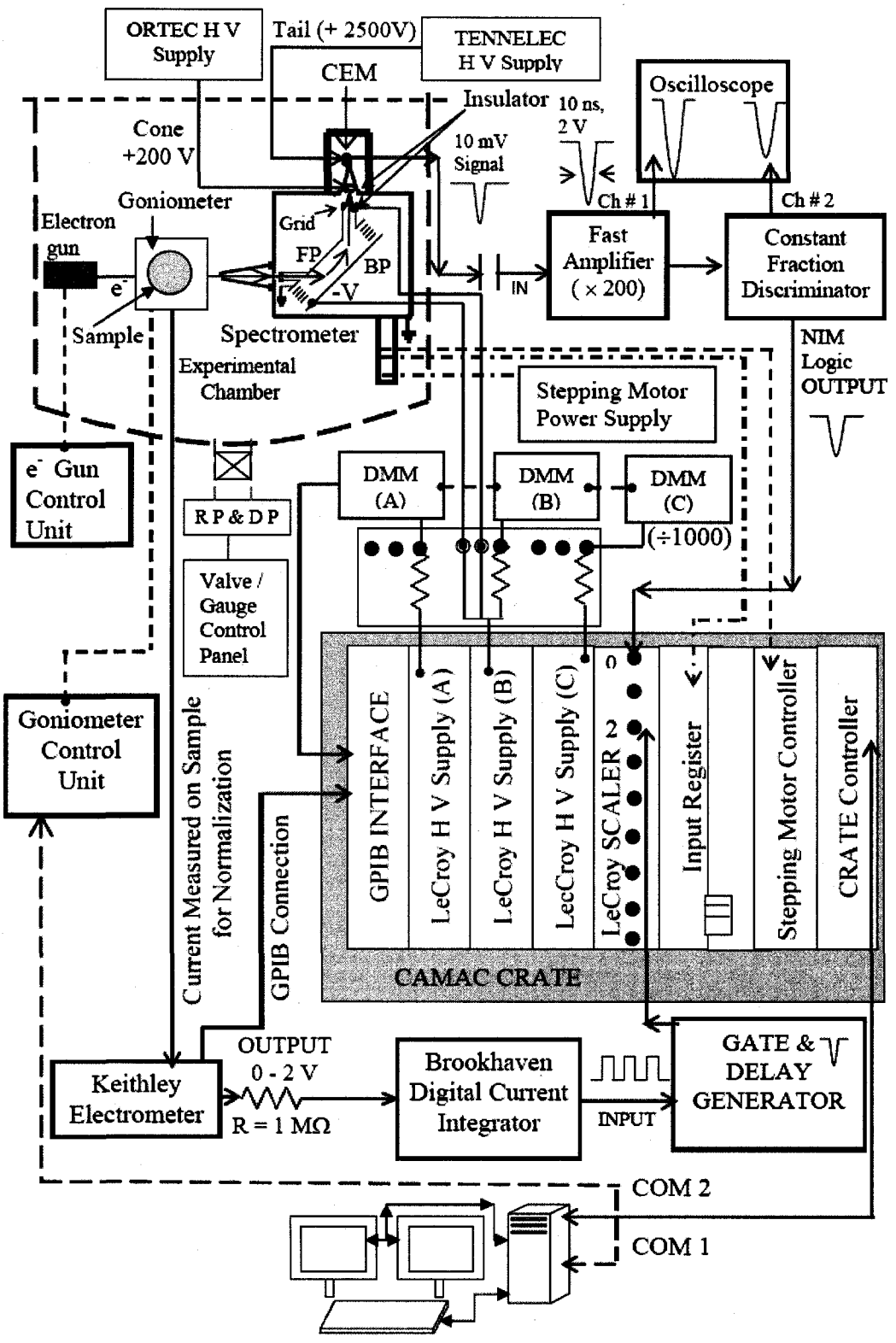

Figure 8. Block diagram of the electronics used.

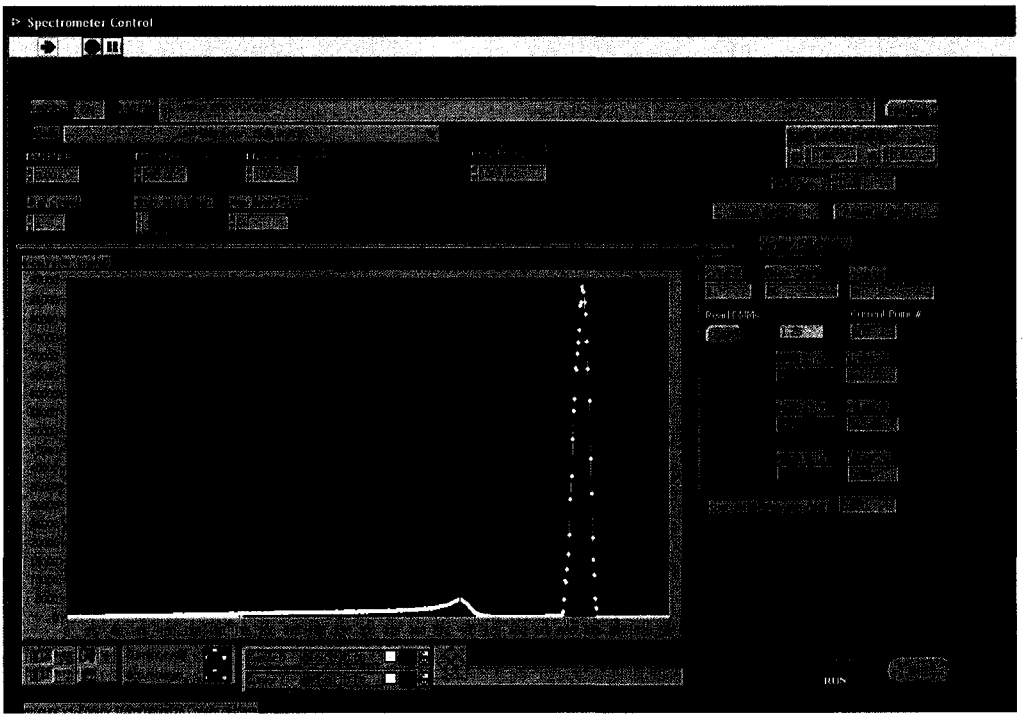

Figure 9. Control panel of the spectrometer and data acquisition interface. A typical electron energy spectrum is also shown.

CHAPTER V

ELECTRON GUDING THROUGH PET NANOCAPILLARIES

In this chapter the guiding of fast electrons (500 and 1000 eV) through insulating polyethylene terephthalate (PET or Mylar) nanocapillaries of length (L) 10 μm and diameter (D) 200 nm (aspect ratio, $\xi = L/D = 50$) is discussed. The measurements focus on the dependence of electron guiding on the foil tilt angle ψ and the incident electron energy. The dependence of the transmitted electron angular distributions on ψ demonstrates that electrons are guided through the capillaries, a result similar to positive ions [37]. However, unlike positive ions [37—58, 67, 68, 71, 73, 74] and slower electrons [59, 82], the spectra of transmitted electrons show significant energy losses for which the fraction of electrons losing energy increases with foil tilt angle ψ and incident electron energy. These energy losses suggest that electrons undergo inelastic scattering within the capillaries before being transmitted or lost inside the foil, a phenomenon not observed to date for ion guiding [37]. Despite the considerable energy losses, it has been found that the inelastically as well as the elastically scattered electrons are guided through the capillaries. The present results indicate that electron and ion guiding are qualitatively and quantitatively different processes. The measurements were later repeated at 500 eV using the same PET sample to cover the full transmitted electron energy range and to validate the guiding and the associated energy losses. A large reduction in the magnitude of the transmitted intensities and a greater fall-off with increasing tilt angle were observed, suggesting deterioration of the sample since the first measurements. Studies of the same PET sample with fast highly charged 16 MeV O^{5+} ions show that the transmitted

ions undergo significant energy losses and charge exchange within the sample, supporting the hypothesis of deterioration of the sample.

PET is a wide band gap insulating polymer [86]. The chemical formula of PET is $(C_{10}H_8O_4)_n$, where n is the degree of polymerization ($\sim 10^3$-10^5) and its IUPAC (International Union of Pure and Applied Chemists) nomenclature is polyoxyethyleneterepthaloyl [86, 87]. It is a "heterochain" polymer since the carbon atoms in the backbone are replaced by oxygen atoms and it belongs to the polyester category [86]. This polymer is either partially crystalline or amorphous and never crystallizes completely due to various chain entanglements [86]. In PET all three phases, e.g., crystalline, non-crystalline, and amorphous, coexist simultaneously [86]. Some of the properties of PET are given in Table 2 [86—89]. Figure 10 shows the chemical structure of a PET polymer [86]. The ionization potentials (valence shell) of hydrogen, carbon, and oxygen atoms and the K-shell ionization energies of carbon and oxygen atoms are listed in Table 3 [86—88].

The PET foils used in this work were prepared at the Hahn-Meitner-Institute, Berlin. A PET foil of thickness 10 μm was first irradiated by high energy ($\sim$ 300 MeV) Kr or Xe ions. The resulting nuclear tracks were then etched uniformly with NaOH to create capillaries of the required dimension. Finally, a 30 nm gold layer was evaporated at an angle 45° onto both sides (entrance and exit) of the capillary foil to prevent the incident ions from building charge up on the surfaces. A schematic diagram of the sample preparation process is shown in Figure 11. A typical PET capillary of aspect ratio 50 and the corresponding scanning electron micrograph (SEM) of the sample are shown in Figures 12 and 13, respectively. The track density of the PET foil that was used is $\sim 10^8$ cm^{-2}. The nominal capillary opening or full

width at half maximum (FWHM) due to the capillary aspect ratio is $\Gamma_{aspect} = \alpha/2 = \frac{200nm}{2\times 10,000nm} \times 57.12 = 0.57^{\circ}$.

Table 2: Properties of PET.

Properties	Value
Density	1.3-1.4 gm/cm^3
Dielectric constant @ 1 MHz	3
Band gap (E_g)	4.13 eV
Electrical resistivity	~ 10^{15} Ω-cm
Electron affinity (χ)	3.22 eV
Work function: $W_{\varphi} = \frac{E_g}{2} + \chi$	5.28 eV
Ionization potential	9 eV
Breakdown voltage for capillaries	1 keV

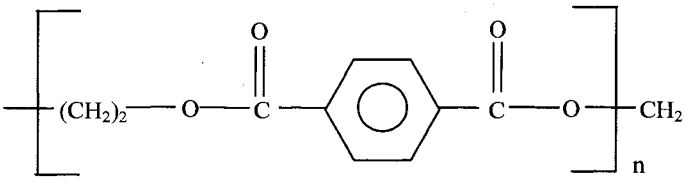

Figure 10. Chemical structure of PET.

Table 3: Valence and K-shell ionization energies of H, C and O atoms.

Elements	Ionization Potential (Valence shell)/ K-shell Ionization Energy (eV)
H^1	13.6
C^6	11.26 / 284.2
O^8	13.6 / 543.1

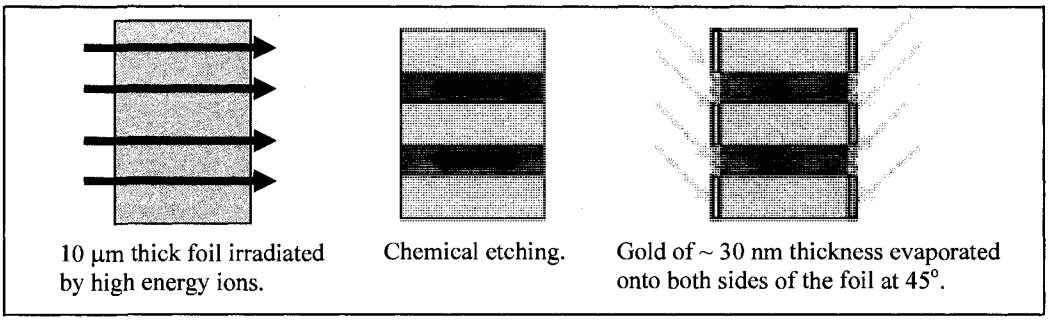

Figure 11. PET sample preparation.

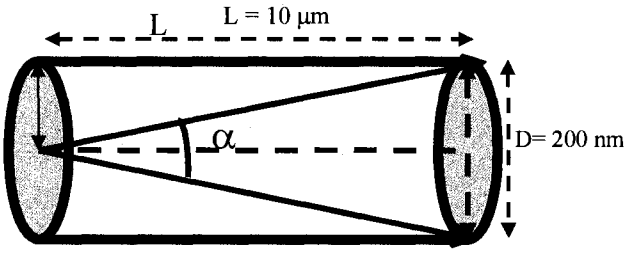

Figure 12. A PET nanocapillary of aspect ratio 50.

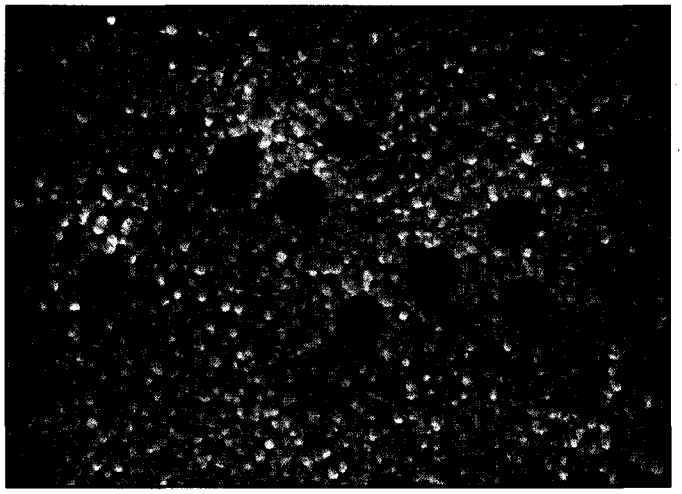

Figure 13: SEM of the PET sample used in the present work.

Results and Discussion

Electron Guiding Through PET

Divergence and Angular Distributions of Electron Beam Without the Sample

The electron beam was collimated to diameter of 1.5 mm. To calculate the mean divergence of the electron beam, maximum and minimum divergences were determined for the electron beam coming from the bare filament (without sample) and were found to be $\Gamma_{coll}^{min} = \frac{1}{2}\left(\frac{d}{l} \times 57.12°\right) = 0.17°$ and $\Gamma_{coll}^{max} = 0.35°$, respectively as shown in Figure 14. Therefore, the beam collimation was estimated as $\Gamma_{coll} = \frac{\Gamma_{coll}^{min} + \Gamma_{coll}^{max}}{2} = 0.25°$.

The angular distributions of 500 and 1000 eV electrons from the bare filament were determined by changing the observation angle (θ) and integrating the recorded spectra at each θ as shown in Figure 15. The FWHM was found to be $\sim 2.7° \pm 0.4°$ for both 500 and 1000 eV electrons.

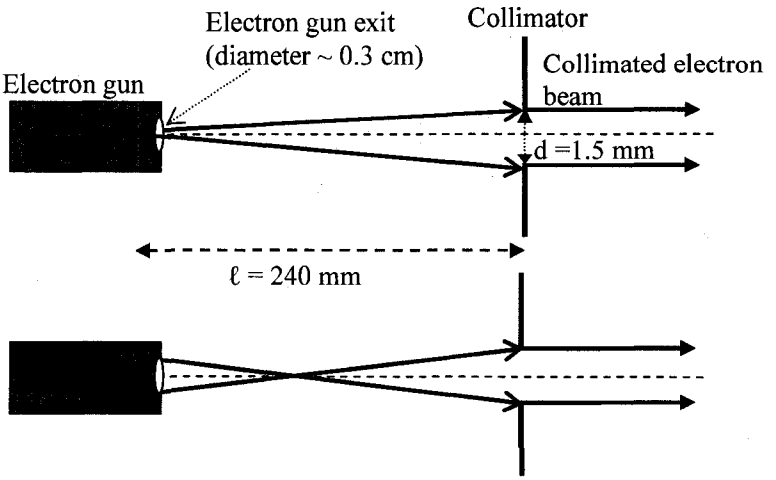

Figure 14. Minimum (upper panel) and maximum (lower panel) divergences of the electron beam.

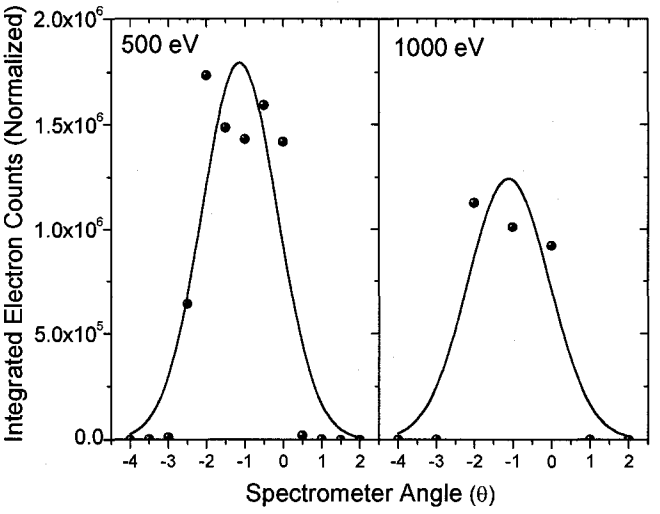

Figure 15. Angular distributions of 500 and 1000 eV electrons from bare filament.

Sample Geometry

The 'zero position' (defined as $\psi = \theta = 0^{\circ}$) of the sample was first located by finding the maximum transmission of electrons directly through the sample along the capillary axis by varying the capillary tilt angle ψ, azimuthal rotation φ, and observation angle θ in small steps. When this zero position was located, the

observation angle was kept at $\theta = 0^{\circ}$ and the tilt angle was varied in small steps to determine the profile for direct transmission of electrons through the foil. This profile determines the minimum ψ at which guiding can be observed for a given sample (Figure 16). The full width at half maximum (FWHM) was found to be $\Gamma_{direct} = 0.65^{\circ}$, showing that direct transmission of electrons through the sample falls very fast. The dependence of direct transmission on tilt angle was also calculated using simple geometric considerations as discussed below[1].

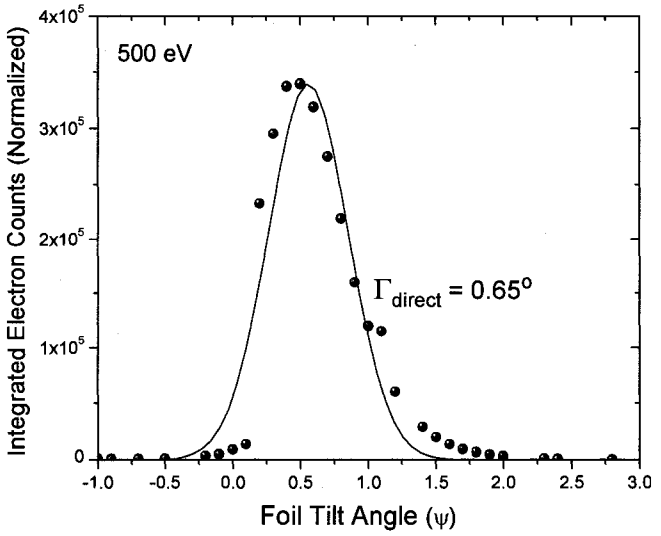

Figure 16. Transmitted electron intensity at $\theta = 0^{\circ}$ for direct transmission of 500 eV electrons as a function of foil tilt angle ψ.

Figure 17 shows the positions of the sample at $\psi = 0^{\circ}$ and $\psi > 0^{\circ}$, respectively. At $\psi = 0^{\circ}$ the beam is transmitted (direct transmission) through the capillaries without any interaction with the inner surfaces of the capillaries (Figure 18). When the foil is tilted ($\psi > 0^{\circ}$) away from its zero position the direct transmission decreases (Figure 19) and finally drops to zero (Figure 20) indicating the

[1] CRC Concise Encyclopedia of Mathematics by E. W. Weisstein

point at which guiding of electrons through the sample can first be observed. The shaded portion in Figure 19 shows the direct transmission of the beam at $\psi > 0°$ which is the overlap of the $\psi = 0°$ and $\psi > 0°$ positions of the sample.

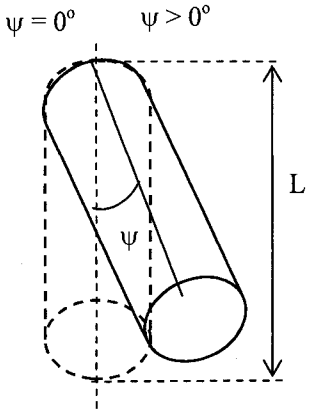

Figure 17. Top view showing the effect of varying ψ.

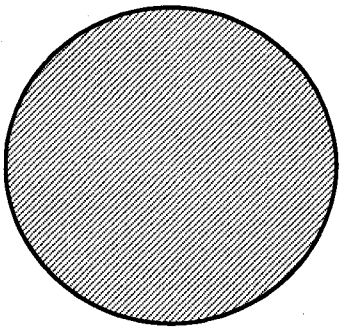

Figure 18. Frontal view of direct transmission of electron beam at $\psi = 0°$.

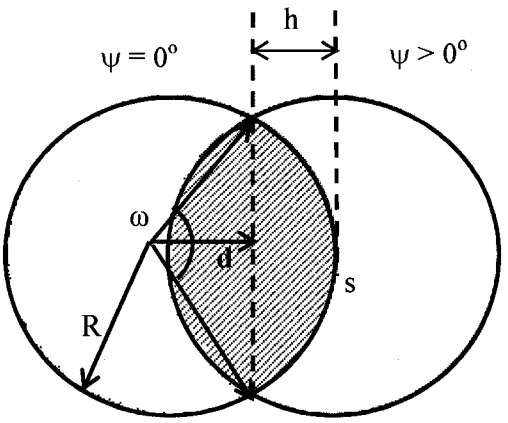

Figure 19. Partial overlap (shaded portion) of $\psi = 0^o$ and $\psi > 0^o$ positions.

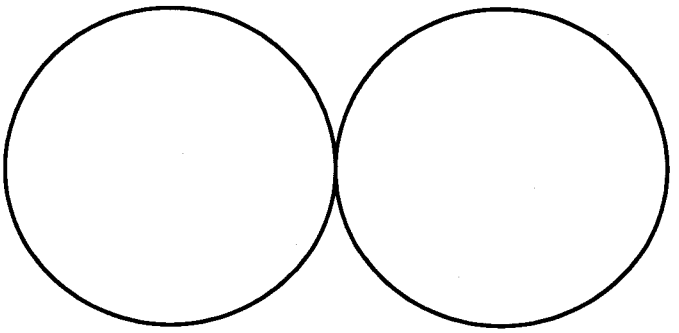

Figure 20. No direct transmission.

From the Figure 19, we have, $R = h + d$; $s = R\omega$ and $Cos\left(\frac{\omega}{2}\right) = \frac{d}{R} \Rightarrow \omega = 2Cos^{-1}\left(\frac{d}{R}\right)$

Therefore, the overlapping area is $A = 2\left[R^2 Cos^{-1}\left(\frac{d}{R}\right) - d\sqrt{R^2 - d^2}\right]$

For, $d = 0, A = \pi R^2 \Rightarrow$ maximum direct transmission; and for

$d = R$, $A = 0 \Rightarrow \psi = \frac{2 \times d}{L} = \frac{2 \times 100}{10,000} \times 57 \approx 1.14°$ for which direct transmission falls to zero.

Therefore, from this geometrical calculation, $\Gamma_{direct} = 0.57^{o}$, which is very close to the experimentally determined value. The experimental width ($\Gamma_{direct} = 0.65^{o}$) is related to the half-widths due to the aspect ratio (nanocapillary nominal opening, $\Gamma_{aspect} = 0.57^{o}$), the beam collimation (divergence of beam, $\Gamma_{coll} \sim 0.25^{o}$), and the degree of parallelism (Γ_{par}) of the nanocapillaries inside the foil by the following convolution formula [90]:

$$\Gamma_{direct} = \sqrt{\Gamma_{aspect}^2 + \Gamma_{par}^2 + \Gamma_{coll}^2} \, .$$

Substituting the measured and calculated values we find that $\Gamma_{par} \sim 0.2^{o}$, indicating a high degree of alignment of the capillaries inside the foil.

It should be noted that for a capillary of length (L) 10 μm and diameter (D) 0.2 μm, i.e., aspect ratio ($\xi = L/D$) of 50, the maximum transmission angle is $\sim 1.14^{o}$ for electrons traveling on a straight line path without touching the inner wall of the capillary. Therefore direct transmission of electrons (without being guided) should vanish at 1.14^{o}. The experimentally determined Γ_{direct} (0.65^{o}) is slightly larger than the geometrical (0.57^{o}) value because of the contributions from nonparallelism ($\Gamma_{par} = 0.2^{o}$) of the capillaries inside the foil and the beam divergence ($\Gamma_{coll} = 0.25^{o}$).

Transmitted Spectra, Angular Distributions, and Energy Losses

Figure 21 shows the energy spectra of the transmitted electrons for the angles $\theta \approx \psi$ (= 0^{o}, 3^{o}, and 5^{o}) for 500 and 1000 eV electrons, respectively. (The spectra exhibit transmitted electrons for energies slightly greater than 500 and 1000 eV due to imprecise calibration of the power supply used to accelerate the electrons.) The spectra for $\psi = 0^{o}$ have nearly the same profile and width as the spectra measured for electrons from the bare filament (i.e., without the sample) as shown by the dashed curves in Figures 21a and 21d, indicating that for $\psi = 0^{o}$ electrons are transmitted

through the foil without interacting appreciably with the capillary walls. The small inelastic contribution on the low energy side of $\psi = 0^{o}$ peak can be attributed to the angular spread of the incident beam and to the capillary nonparallelism, which had FWHM values of ~ 0.25^{o} and ~ 0.2^{o}, respectively as discussed above. As seen from Figure 21, not only does the overall transmitted intensity decreases strongly as the tilt angle increases, the spectra also show significant energy losses for the transmitted electrons, suggesting that a fraction of the incident electrons undergo inelastic scattering with the inner surfaces of nanocapillaries. This energy loss is quite unexpected in view of earlier results for slow positive ions [37] and the recent results for 200 — 350 eV electrons in Al_2O_3 [59] for which no appreciable loss was observed even for rather large tilt angles. Quantification of the energy losses associated with the transmitted spectra is discussed below.

The angular distributions of transmitted electron intensities were calculated by integrating the entire spectrum (450 — 550 eV for 500 eV and 880 — 1100 eV for 1000 eV, respectively, in Figure 21) of electrons transmitted through the sample for 500 and 1000 eV electrons as a function of observation angle θ for several foil tilt angles ψ as shown in Figure 22. The transmitted intensities were normalized to incident beam currents of ~ 0.3 nA and ~ 0.8 nA measured on the sample for 500 and 1000 eV, respectively, and were determined under equilibrium conditions, i.e., after a sufficient time that charge-up effects on the inner walls of the nanocapillaries had reached a steady-state condition [37]. For the present work, the electron beam was typically started 2-3 hours prior to beginning the measurements. In all cases the transmitted intensities were normalized to same number of incident beam particles, so the intensities are plotted as the integrated number of counts rather than as a fraction.

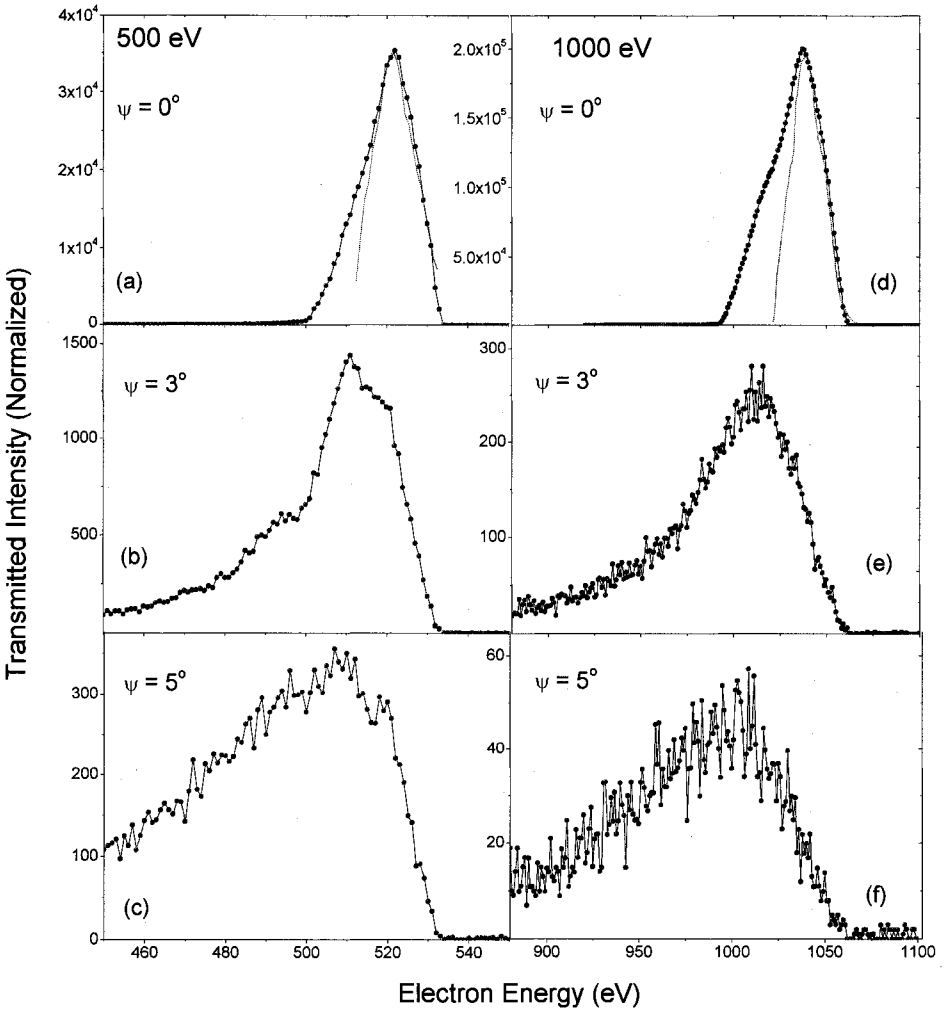

Figure 21. Measured electron energy spectra for angles $\theta \approx \psi$ showing that transmitted electrons undergo significant energy losses. The dashed curves in (a) and (d) show the energy spectra obtained for electron emission from the bare filament normalized to the spectra for $\psi = 0^{\circ}$.

Figure 22 indicates that electrons are guided through the nanocapillaries, a result similar to that for positive ions [37]. A plot of the centroids of the angular distributions vs. foil tilt angles, shown in Figure 23, exhibits a linear relationship with the centroid observation angle nearly coinciding with the foil tilt angle. For instance, when the foil is tilted by 3° the centroid of the corresponding angular distribution is observed close to 3° (the centroids of the angular distributions may not be exactly

equal to ψ in Figures 22 and 23 because of mechanical offsets of ~ 1° in the measured angles) demonstrating that indeed electrons are guided through the nanocapillaries.

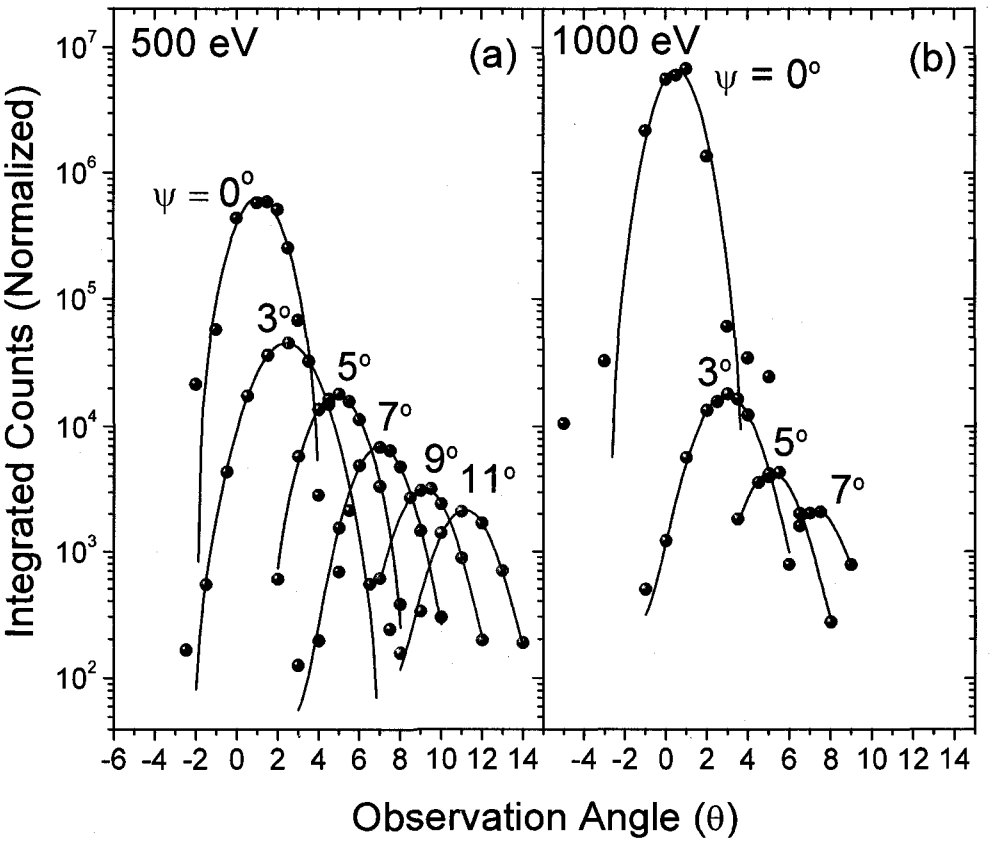

Figure 22. Angular distributions of the normalized integrated transmitted electron intensities plotted as a function of observation angle θ for the indicated tilt angles ψ for (a) 500 eV and (b) 1000 eV incident electrons. Solid lines are Gaussian fits to the data.

Moreover, from Figure 22 it is observed that the intensity of electron guiding depends strongly on the foil tilt angle and the incident electron energy. The guiding decreases exponentially with the foil tilt angle (ψ) and also decreases with incident electron energy (for 500 eV guiding was observed up to $\psi = 11°$, whereas for 1000 eV only up to $\psi = 7°$). These results are similar to those for positive ions [37, 38, 40—43, 45—48, 51—55, 67, 74]. The angular widths of the guided electron distributions shown

in Figure 22 are about 3°, and do not change noticeably with tilt or observation angle. No strong significance should be attached to this result, however, because the inherent angular resolution of the spectrometer was about 2.7° for the collimated 500 eV electron beam (nearly the same value was found for 1000 eV) observed directly from the bare filament.

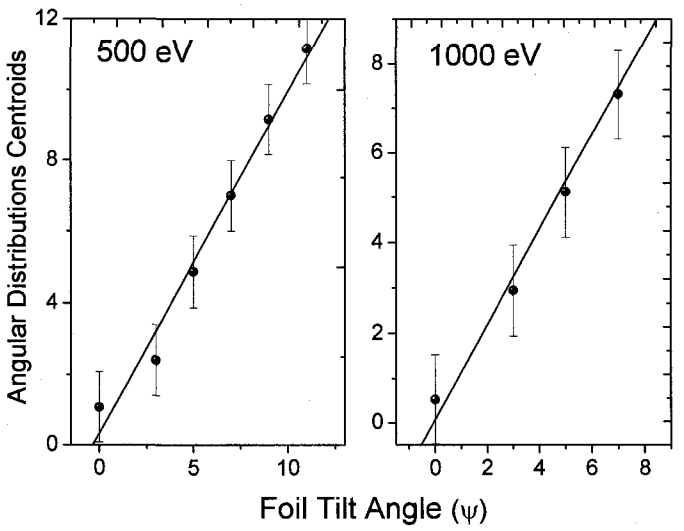

Figure 23. Plots obtained from the data of Fig. 22 showing the centroids of the angular distributions vs. the foil tilt angles (ψ) for 500 and 1000 eV incident electrons. The linear dependence demonstrates that electrons are guided through the PET nanocapillaries.

The angular distributions for direct transmission at $\psi = 0^{\circ}$ for 250, 500 and 1000 eV incident electrons plotted in Figure 24 show that transmitted intensity increases exponentially with increasing electron energy (see inset of Figure 24).

To quantify the energy losses, the elastic and inelastic contributions to the transmitted electron intensity, denoted by $I_{elastic}$ and $I_{inelastic}$, respectively, were evaluated separately. As noted above (see Figure 21) the spectra of 500 and 1000 eV electrons show that for $\psi = 0^{\circ}$ electrons are transmitted through the foil encountering only minimal interactions with the capillary walls. Consequently, any deviation from

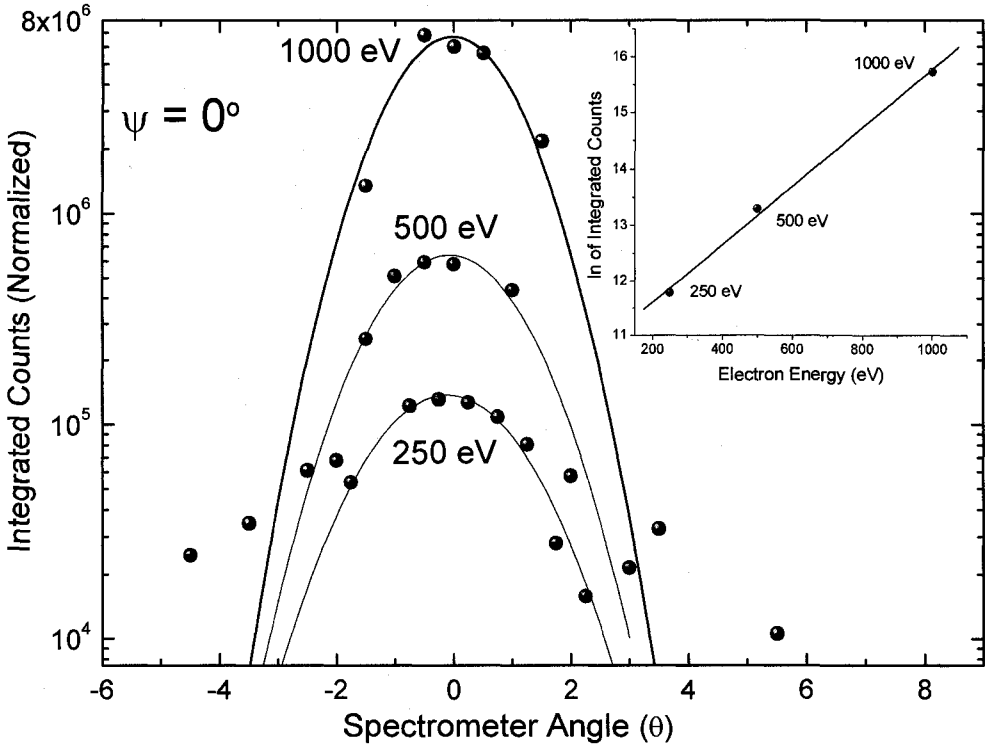

Figure 24. Angular distributions for direct electron transmission at $\psi = 0^{\circ}$ at incident electron energies of 250, 500 and 1000 eV.

the measured $\psi = 0^{\circ}$ energy profile for tilt angles $\psi > 0^{\circ}$ is significant. This deviation can be determined by superimposing the spectrum for $\psi = 0^{\circ}$ on the corresponding spectra for $\psi > 0^{\circ}$ and normalizing to the intensities of these latter spectra. When this is done it is found that the high energy cutoff of the spectra for $\psi > 0^{\circ}$ matches that for $\psi = 0^{\circ}$ as shown in Figure 25, indicating the existence of an elastic contribution for all tilt angles. In this way the elastic contribution can be determined directly and the inelastic contribution can be obtained by subtraction of the elastic contribution from the total integrated spectrum.

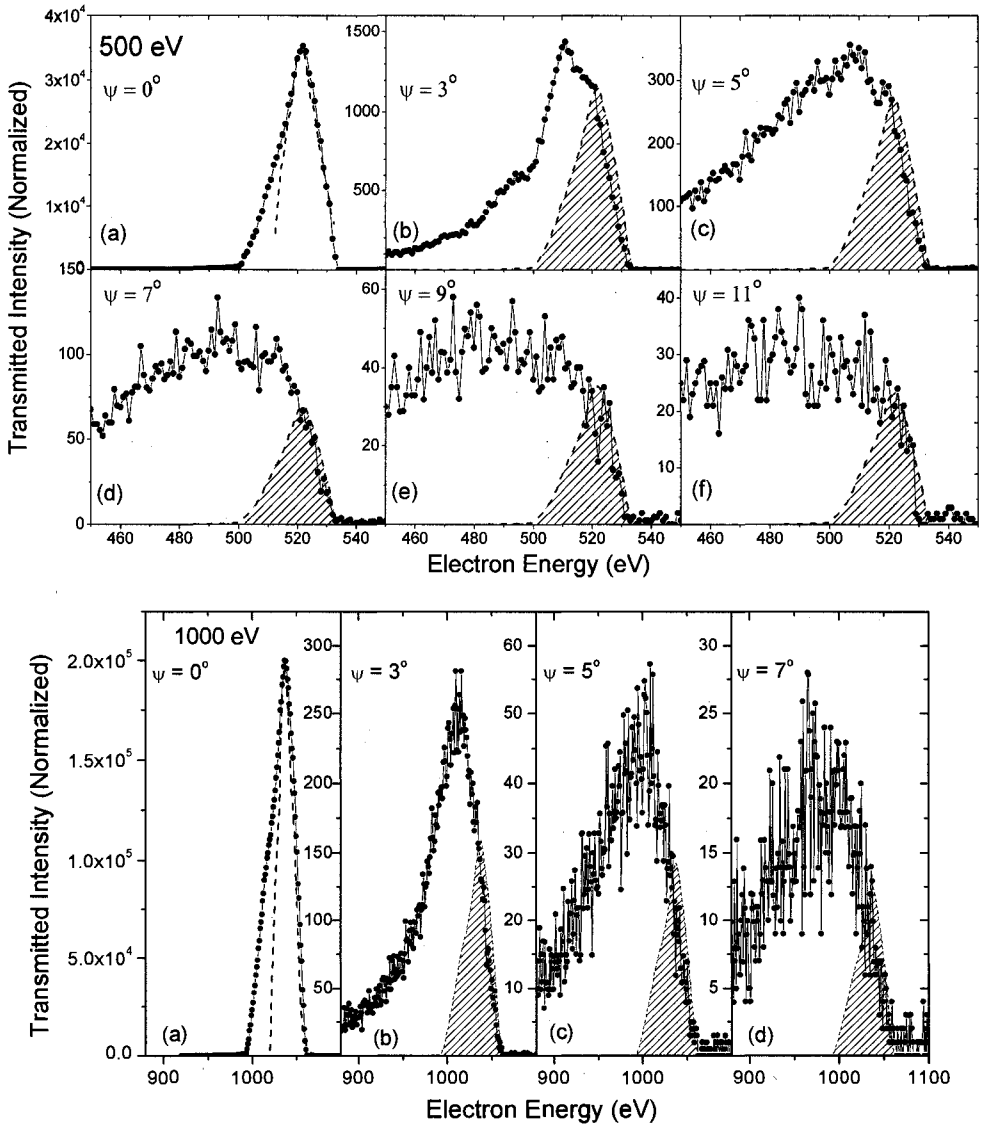

Figure 25. Measured electron energy spectra for angles $\theta \approx \psi$ showing the increasing fractional electron energy loss vs. ψ for incident 500 (upper panels) and 1000 eV (lower panels) electrons. The dashed curve for $\psi = 0^{\circ}$ in each case shows the energy spectrum obtained for electron emission from the bare filament normalized to the spectrum for $\psi = 0^{\circ}$. The shaded areas show the spectrum for $\psi = 0^{\circ}$ normalized to the spectra for $\psi > 0^{\circ}$, indicating the elastic contributions to the individual spectra.

A plot of $\frac{I_{inelastic}}{I_{elastic}}$ vs. tilt angle (ψ) in Figure 26a shows that this inelastic

contribution dominates the transmitted spectra and increases with foil tilt angle. It is

seen that for 500 eV electrons the ratio saturates above about 7°. This is because incomplete electron energy spectra over the region of loss were recorded (see Figure 25), an oversight resulting from the fact that energy losses associated with the transmitted electron spectra were not anticipated based on the earlier results for slow positive ions and lower energy electrons. This omission was later corrected by repeating the measurements at 500 eV.

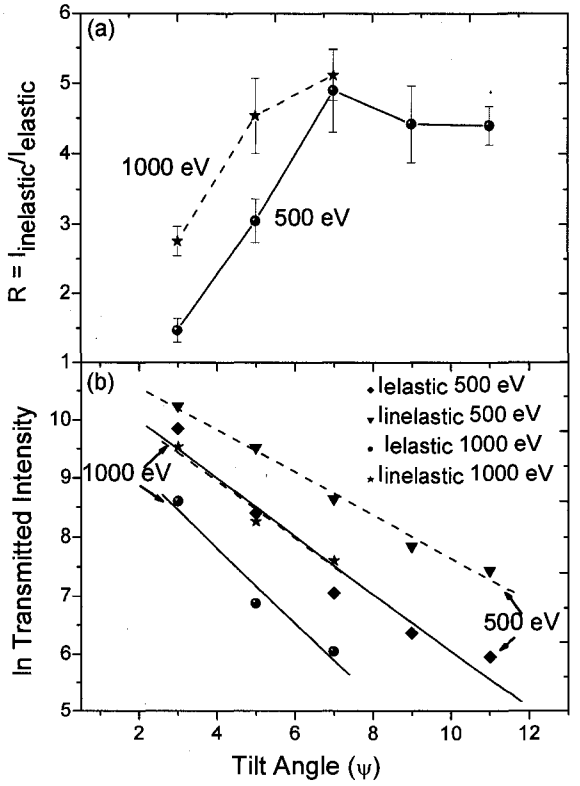

Figure 26. (a) Plot of $\frac{I_{inelastic}}{I_{elastic}}$ as a function of tilt angle (ψ); (b) linear fits to the elastic and inelastic contributions to the transmitted intensities for incident 500 and 1000 eV electrons.

Guiding Ability of the Capillaries

The ability of the capillaries to guide the ions or electrons is known as the *characteristic guiding angle* ψ_c defined as the angle at which transmitted intensity

falls to $\frac{1}{e}$ of its value at $\psi = 0°$, i.e., $\frac{f(\psi_c)}{f(0)} = \frac{1}{e}$ [46, 51–53]. To determine ψ_c, the spectra for electron observation angles $\theta \approx \psi$ (i.e., the centroid observation angle for each ψ) shown in Figure 25 were considered, since these spectra represent the maximum transmitted intensity for each tilt angle. To separately determine the values of ψ_c corresponding to the elastic and inelastic contributions associated with the transmitted electron spectra, the natural logarithm of the elastic and inelastic contributions were taken and then plotted vs. ψ as shown in Figure 26b. It was found that these values can be fit by a linear function

$$Y = G - H * X\left[\equiv \left\{ \ln I(\psi) = \ln I(0) - \frac{\psi}{\psi_c} \right\} \right]. \qquad 10$$

The inverse of the slope H then gives the corresponding value of ψ_c and G gives the intercept. From Equation 10 the transmission of electrons through PET nanocapillaries then follows an exponential attenuation law of the form

$$I(\psi) = I(0^\circ)\exp\left(-\frac{\psi}{\psi_c}\right), \qquad 11$$

rather than $f(\psi) = f(0)\exp\left(-\frac{\sin^2\psi}{\sin^2\psi_c}\right)$ (see Equation 5, Chapter III) found for slow highly charged ions [37, 46–48, 51–53] and lower energy electrons [59]. The values of ψ_c for the elastic and inelastic contributions are given in Table 4 and compared with the results obtained by Hellhammer *et al.* [46, 47] for positive ions. It is seen that the values of ψ_c obtained in the present work for electrons are smaller than the corresponding values for ions, and, furthermore, the values of ψ_c are quite different for the elastic and inelastic contributions. Table 4 quantitatively suggests that electron guiding falls faster than for ion guiding, i.e., the guiding ability of capillaries is

smaller for electrons than for ions. Moreover, a comparison of Equations 5 and 11 indicates that the guiding mechanism associated with electrons transmitted through nanocapillaries is different than for ion guiding [91].

Table 4: Values of ψ_c for electrons and comparison with positive ions.

	ψ_c (degrees)		
E/q (V)	Elastic	Inelastic	Ions [46, 47]
500	2.0 ± 0.3	2.8 ± 0.15	4.7
1000	1.6 ± 0.3	2.1 ± 0.35	2.9

To represent the integrated measured intensity for all tilt angles including $\psi = 0^\circ$, a *direct* contribution representing the large transmission fraction near $\psi = 0^\circ$, corresponding to electrons passing through the capillaries with negligible interactions with the capillary walls, must be included. From geometrical considerations, this contribution, which is due to the convolution of the capillary aspect ratio, the beam collimation, and capillary nonparallelism, decreases nearly linearly for $\psi > 0^\circ$ as discussed above. To quantify the fast fall-off of the direct transmission, the characteristic guiding angle ψ_c^{direct} was determined. For this, the values for the elastic ($G_{elastic}$) and inelastic ($G_{inelastic}$) contributions at $\psi = 0^\circ$ were determined from the intercept values G in Equation 10. These two values were then subtracted from the total contribution at $\psi = 0^\circ$ to determine the direct contribution $I(0^\circ)_{direct}$. The Equation. 11 was then used to determine the ψ_c^{direct} giving a value of $\sim 0.16^\circ$ for both

500 and 1000 eV electrons, indicating that direct transmission decreases very rapidly as expected as shown in Figure 27.

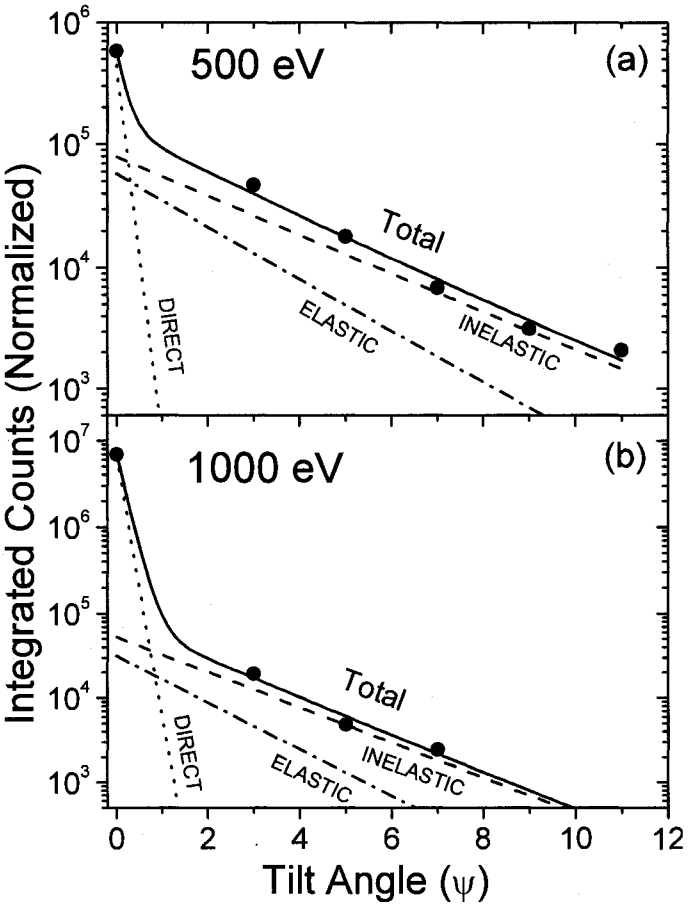

Figure 27. Relative transmission intensities vs. tilt angle for 500 and 1000 eV electrons.

Angular Distributions of Elastically and Inelastically Scattered Electrons

Using the same analysis technique for all observation angles θ for a given tilt angle ψ, the elastic and inelastic contributions associated with each transmitted spectrum for $\theta \neq \psi$ were evaluated separately as shown in Figure 28 at $\psi = 9^{o}$ for 500 eV electrons. The resulting angular distributions plotted in Figure 29 show that the centroids of the elastically and inelastically scattered electrons coincide and are nearly equal to the tilt angle, i.e., $\theta \approx \psi$, demonstrating convincingly that inelastically as well

as elastically scattered electrons are guided through the capillaries. These results again show that the inelastic contributions dominate and that the elastic contributions fall faster than the inelastic ones. The results from Figure 22 for the integrated transmitted intensities are again shown in Figure 29 for comparison.

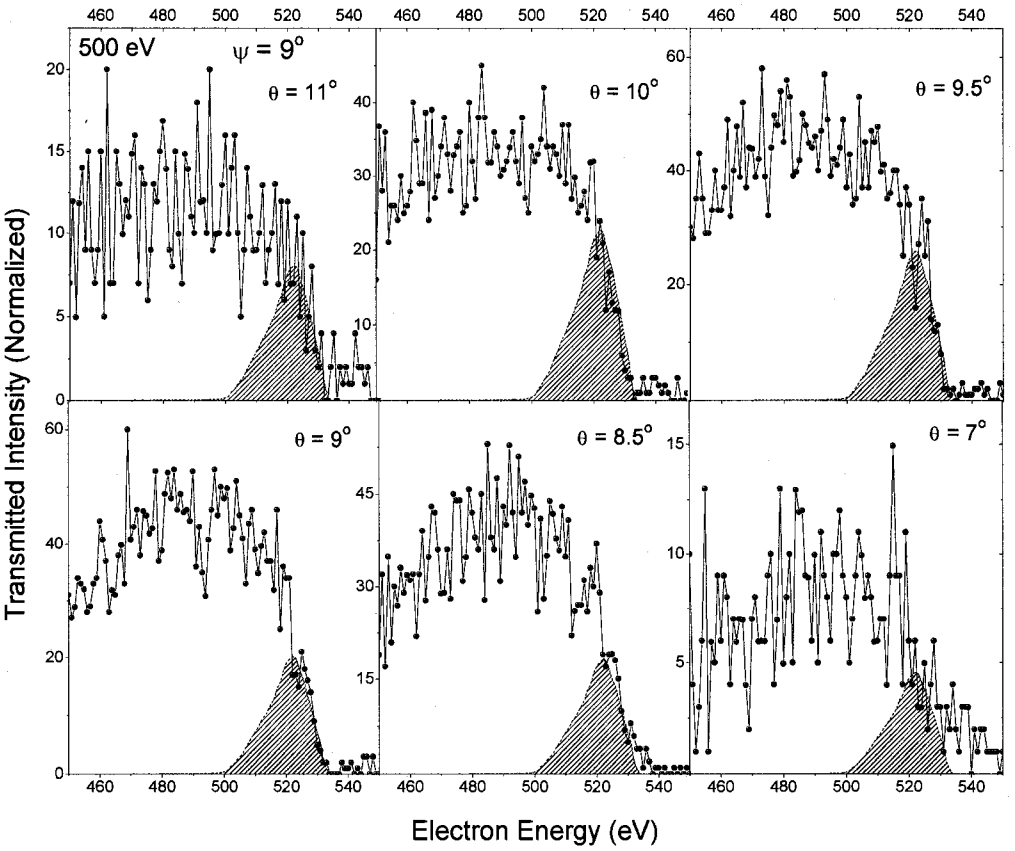

Figure 28. Determination of elastic and inelastic contributions for all observation angles at $\psi = 9^{\circ}$ for 500 eV electrons.

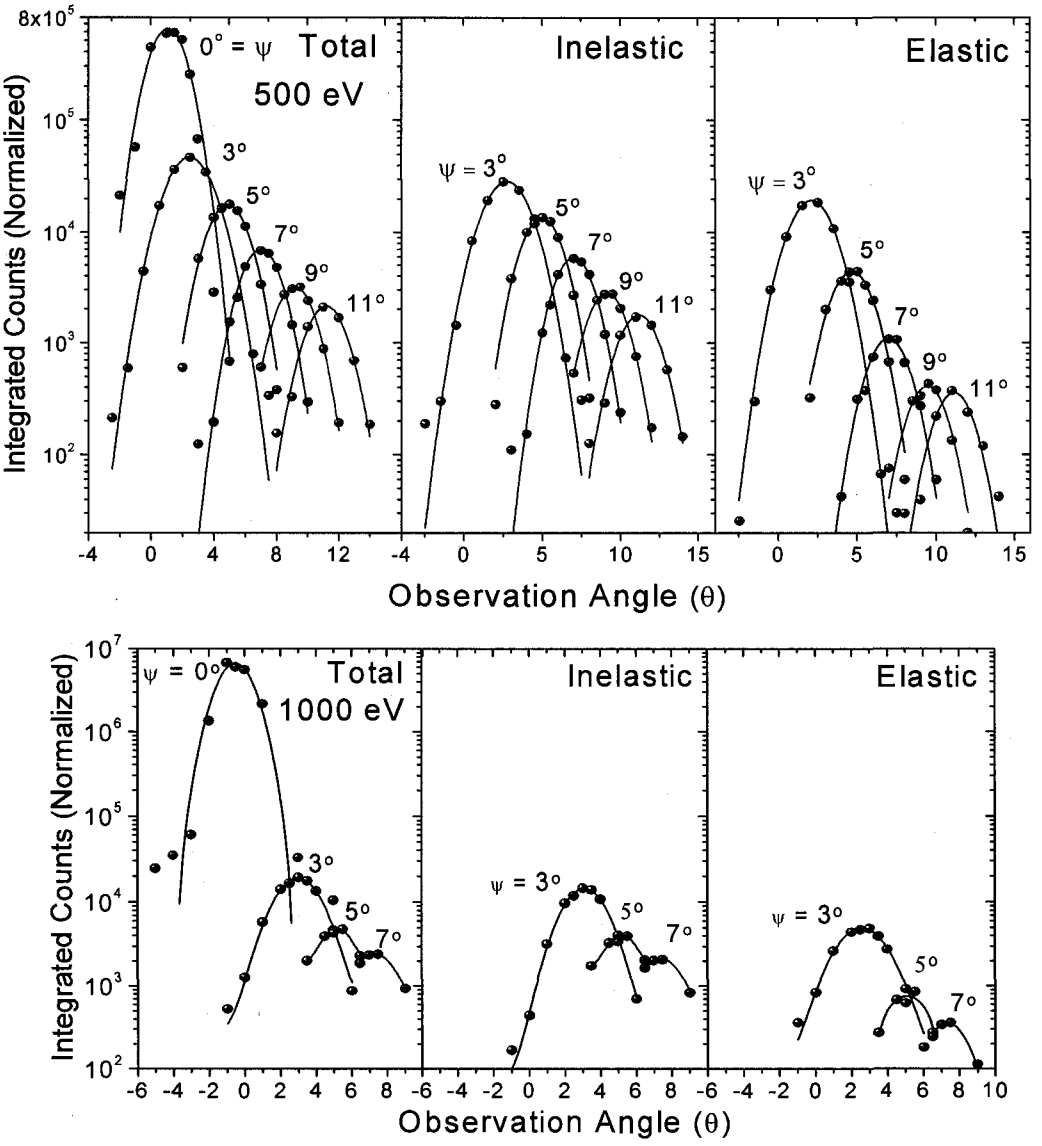

Figure 29. Angular transmission profiles for the inelastic and elastic contributions to the measured electron energy spectra for each tilt angle investigated.

Repetition of the Measurements at 500 eV and Possible Deterioration of Sample

The measurements were repeated for the transmission of 500 eV electrons through the same insulating PET nanocapillary sample (length 10 μm and diameter 200 nm) used to obtain the results already described above. The intent of these new measurements was to cover the entire energy range of transmitted electrons, i.e., the

complete range of energy loss, to confirm the previously observed energy losses in the transmitted electron spectra (see upper panels b, c, d, e, f of Figure 25), and to confirm the apparent guiding of inelastically scattered electrons (see Figure 29).

In the earlier measurements, the regions of the spectra corresponding to the energy losses were incomplete because such losses were not anticipated based on the previous results for slow ions [37], and for electrons [59] with energies similar to those used here. Consequently, the spectra were not collected for sufficiently low electron energies. In the new measurements for 500 eV electrons, the spectra were recorded for transmitted electron energies from 350 to 550 eV to correct this omission. In addition to confirming the essential features of the earlier measurements, a significant deterioration of the sample apparently occurred as manifested in substantially reduced transmission intensities and a greater fall-off of these intensities with foil tilt angle as discussed below.

Figure 30 shows the energy spectra of the transmitted electrons for tilt angles 4°, 8°, and 12° and $\theta = \psi$. These spectra cover the full range of electron energy loss as opposed to those of Figure 25. The transmitted electron spectra for $\psi > 0^{\circ}$ (Figures 30b, c, d) show significant energy losses, indicating again that a large fraction of the incident electrons undergo inelastic scattering with the inner surfaces of the nanocapillaries in agreement with previous observations.

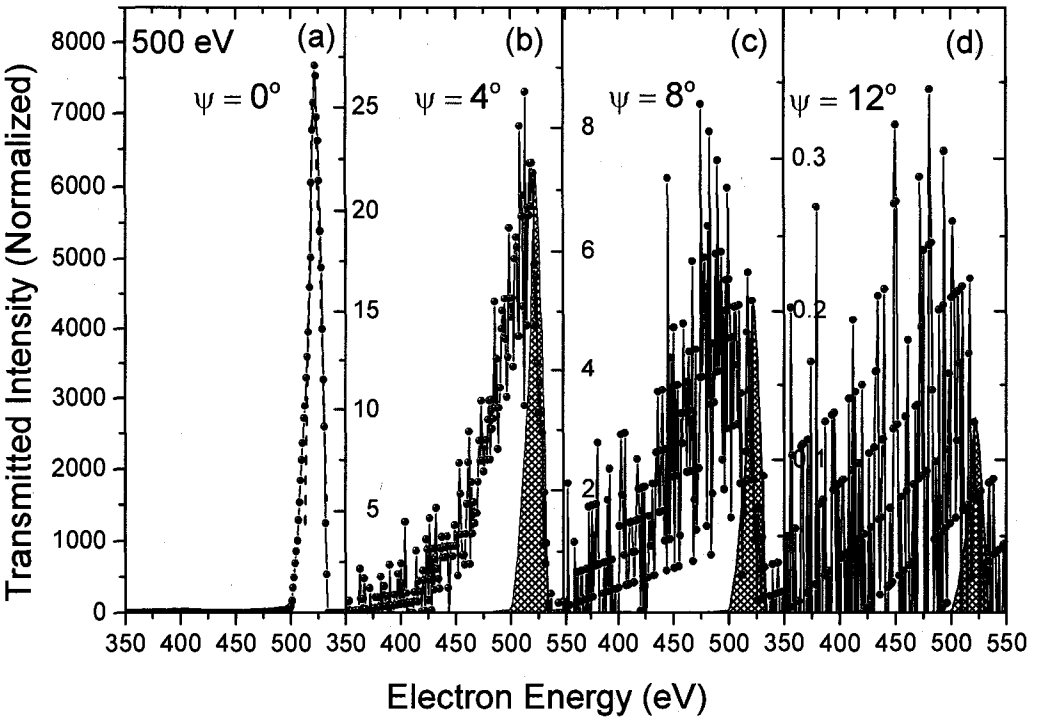

Figure 30. Repeated measurements of electron energy spectra for angles $\theta \approx \psi$ again showing that transmitted electrons undergo significant energy losses. The dashed curve in (a) shows the energy spectrum obtained for electron emission from the bare filament normalized to the spectrum for $\psi = 0^{\circ}$. The shaded areas in (b)-(d) show the spectrum for $\psi = 0^{\circ}$ normalized to the spectra for $\psi > 0^{\circ}$, indicating the elastic contribution to the individual spectra.

The angular distributions of the transmitted intensities were calculated by integrating the entire spectrum (350 — 550 eV), after background subtraction, for each recorded observation angle θ at a given tilt angle ψ, to obtain the results shown in Figure 31a. For comparison, the corresponding results from Figure 22a for the same PET foil are shown in Figure 31b. The transmitted intensities were normalized to the incident beam current of ~ 0.5 — 3.0 nA as measured on the sample, and were determined under equilibrium conditions as before. As seen from Figure 31a, the transmitted intensities in the later measurements are significantly lower than those of

the earlier measurements for the same PET foil (Figure 31b), suggesting changes in the sample properties or deterioration of the sample.

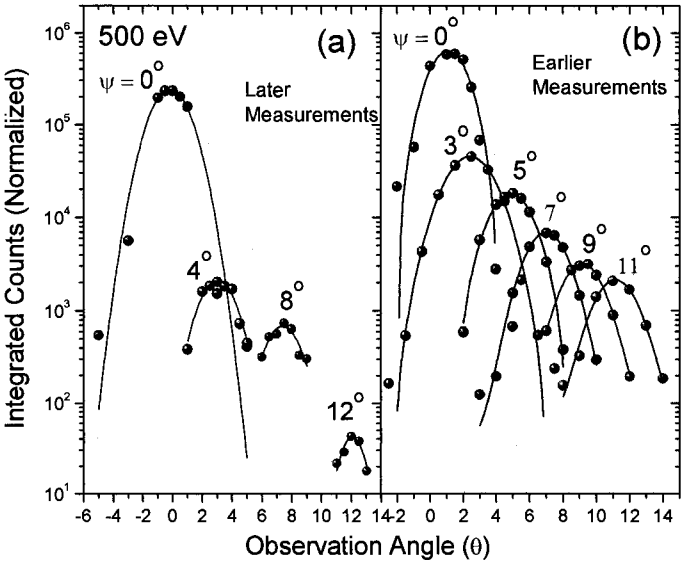

Figure 31. Angular distributions of the integrated normalized transmitted electron intensities as a function of observation angle θ for the indicated foil tilt angles ψ for 500 eV incident electrons for the later and earlier measurements. Solid lines are Gaussian fits to the data.

The elastic ($I_{elastic}$) and inelastic ($I_{inelastic}$) contributions associated with each of the transmitted spectra were evaluated separately by superimposing and normalizing the $\psi = 0^o$ spectrum onto the $\psi > 0^o$ spectra as shown in Figures 30b-30d, following the technique used in Figure 25. The shaded areas show the elastic contributions. The inelastic contribution was then determined by subtracting the elastic contribution from the total integrated intensity of the spectrum. The ratio $\frac{I_{inelastic}}{I_{elastic}}$ plotted as a function of foil tilt angle ψ in Figure 32, which includes the measurements, shows that inelastic contributions dominate the transmitted electron energy spectra with the relative contribution increasing over the full range of the measured ψ, and with the ratios for

500 eV still being a little bit lower than for 1000 eV. For the earlier 500 eV data the ratio saturated above about 7° because of the incomplete electron energy spectra that were recorded (see Figure 25).

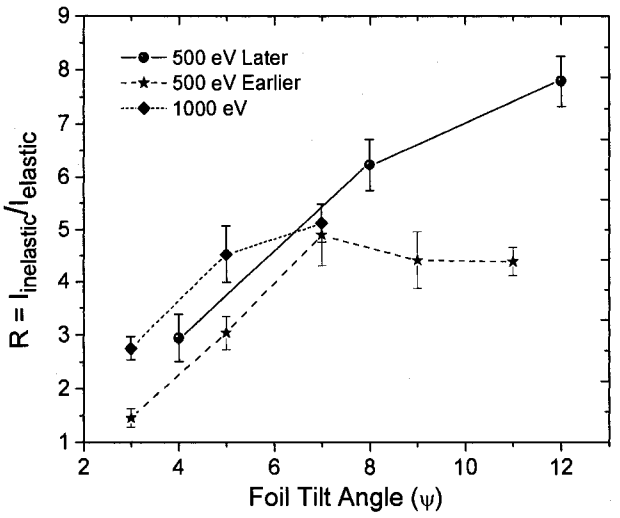

Figure 32. Plot of $\frac{I_{inelastic}}{I_{elastic}}$ as a function of tilt angle ψ for 500 eV electrons for the earlier and later measurements, and for 1000 eV electrons showing that the inelastic contribution dominates the transmitted electron intensity and increases with ψ and increasing electron energy.

Using the same analysis technique for all observation angles θ for a given tilt angle ψ, the elastic and inelastic contributions associated with each transmitted spectrum for $\theta \neq \psi$ were again separately evaluated. From the resulting angular distributions of inelastically and elastically scattered electrons shown in Figure 33, it is seen that the centroids coincide and are nearly equal to the tilt angle, i.e., $\theta \approx \psi$, demonstrating that inelastically as well as elastically scattered electrons are guided, an observation similar to that of Figure 29.

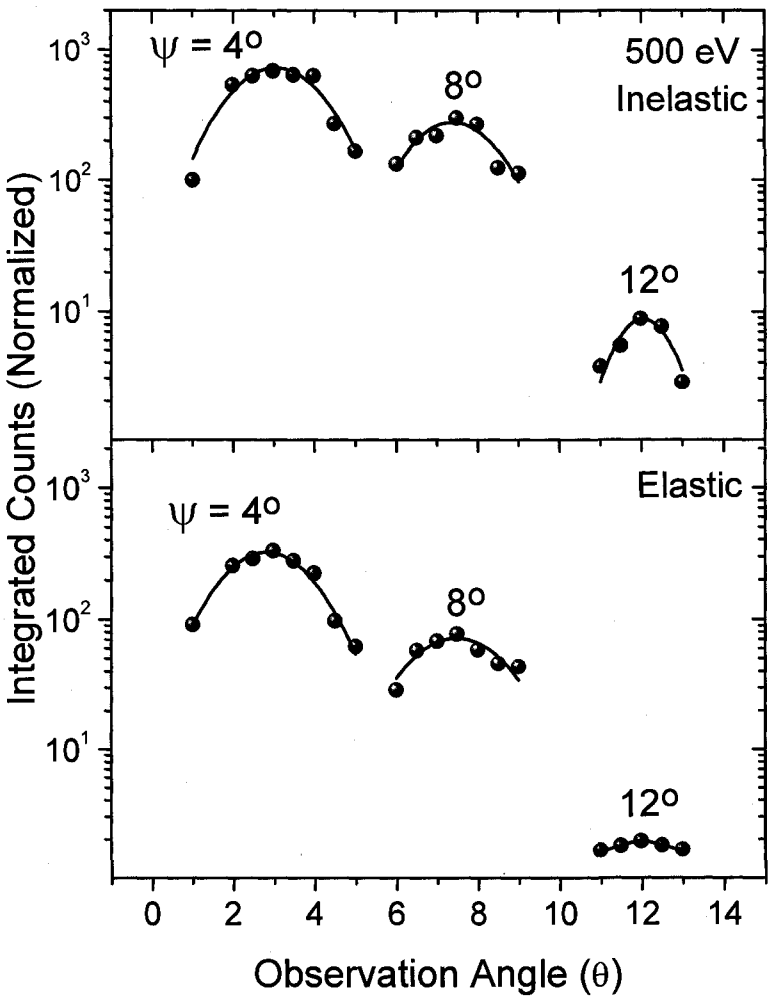

Figure 33. Angular distributions of inelastically and elastically transmitted electrons for the later measurements using the same PET nanocapillary foil.

The *characteristic guiding angle* ψ_c [46] based on Equation 11 for the elastic and inelastic contributions were then separately determined following the same technique as before and are listed in Table 5 along with the previous values (see Table 4) obtained. It is seen that the later values of ψ_c are considerably smaller than those obtained earlier.

At this juncture it should be noted that elastic and inelastic scattering of 2 MeV He^+ ions transmitted through a tapered (inlet diameter = 0.8 mm and outlet diameter ~ 0.8 μm) SiO_2 capillary were also observed by Nebiki *et al.* [60] for

capillary tilt angles of 0^{o} and 2^{o}. However, the inelastically transmitted ions were attributed to penetration of the capillary walls and not to guiding. Moreover, only elastic guiding was reported [60] in contrast to the present work for which guiding of both elastically and inelastically scattered electrons transmitted through the PET capillaries has been observed for all foil tilt angles.

Table 5. Values of the characteristic guiding angle ψ_c obtained from the data of Figure 30 for the elastic and inelastic contributions associated with the electron energy spectra compared with the ψ_c values obtained from the data of Figure 25.

ψ_c (degrees)		
E/q (V)	Elastic	Inelastic
500 (Later)	1.4 ± 0.4	1.8 ± 0.7
500 (Earlier)	2.0 ± 0.3	2.8 ± 0.15

The significantly reduced transmitted intensities and greater fall-off with increasing tilt angle for the later measurements suggest deterioration of the sample. Though the exact reasons and the magnitude of deterioration are not known explicitly, likely causes are considered.

One possibility is physical or chemical damage to the sample from long periods of bombardment by the intense beam of electrons during the measurements. The intense electron beam may increase the conductivity of the inner surfaces of capillaries which, in turn, reduce the ability of the capillaries to form and maintain the charge patches in the entrance region for guiding. Another possibility is that contamination on the surface reduced the transmitted intensities by partially blocking the capillaries. The electron beam may partially block the capillaries by depositing the hydrocarbons on the surface of the sample during the bombardment, which, in turn,

reduced the transmitted intensity. In support of this latter hypothesis, visual examination of the sample showed discoloration at the point of impact with the electron beam and a spot size corresponding to the beam size. Such discoloration has been observed by other investigators [52], and was attributed to residual hydrocarbons in the beam line that are deposited on the surface of the sample by impact with the beam. In addition, a diffusion pump was used to pump the chamber and during the measurements the vacuum inside the chamber was ~ 10^{-6} Torr which may also lead to deposition of hydrocarbons on the sample.

Universal Scaling Law

As noted, the intensities of the transmitted electrons, and hence the values of ψ_c, are lower than for positive ions [46, 47], indicating that electron guiding falls faster [see Table 4] than for ions. For slow positive ions a universal scaling law $\sin^{-2}\psi_c = \frac{E_p}{qU_s}$ (Equation 6 of Chapter III) was deduced [46, 47, 53], where E_p and q are the energy and charge state of the incident ions, and U_s is the deflection potential across the capillary diameter in the entrance region. The values of U_s deduced for electrons and ions [46, 47, 53] using this scaling law are listed in Table 6. Although the data for electrons are very limited compared to those for ions [46, 47, 53], it appears that electrons may also follow a scaling law with nearly same slope but a different magnitude (intercept) as shown in Figure 34. From Table 6 it is evident that the deflection potential U_s produced by the electrons in the entrance region of the capillaries is much smaller than for ions, suggesting that, electrons are less efficient at depositing and maintaining charge patches to guide the subsequent incoming electrons through the nanocapillaries.

Table 6. Values of the deflection potential U_s for electrons and ions of the same energy to charge state ratio, as determined from $U_s = \frac{E_p \sin^2 \psi_c}{q}$.

U_s (V)			
E_p/q (V)	Electrons		Ions
	Elastic	Inelastic	[46, 47, 53]
500 (Earlier)	0.6	1.2	3.4
1000	0.8	1.3	2.3

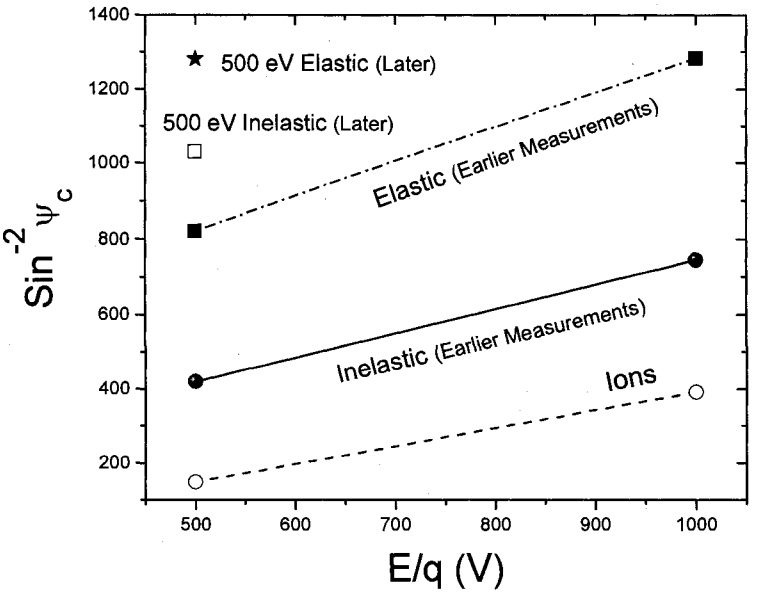

Figure 34. Scaled values of the characteristic guiding angle ψ_c plotted as a function of the projectile energy (in eV) divided by charge state (q) according to Equation 6.

Understanding the Differences Between Electron and Ion Guiding

From Tables 4 and 6 it is seen that for the same energy-to-charge ratio, i.e., E_p/q, the characteristic guiding angle ψ_c and calculated deflection potential U_s for slow HCIs and electrons are quite different. These differences suggest that ions are

more efficient at forming and maintaining charge patches inside the capillaries, and hence are better able to guide subsequent incoming ions. Moreover, the spectra of transmitted ions do not show any significant energy loss or change in the charge state, indicating that these ions do not undergo close collisions with the capillary surface, a condition necessary for guiding the ions through the capillaries [37, 57]. In this regard, it is noted that Monte Carlo simulations [57] for the guiding of slow HCIs also did not show any energy loss or change in the charge state associated with the transmitted ions. Slow HCIs can produce secondary electrons [91, 92] in close encounters with the capillaries [12—14], and can also become fully neutralized, but not those ions which are transmitted through the capillaries as is evident from the observed unaltered charge state of the transmitted ions [37, 40—43, 45—48, 51—58]. Moreover, secondary electrons produced by ions increase the magnitude of the deposited positive charge [92], while secondary electrons resulting from electron bombardment decrease the charge.

The smaller values of ψ_c (Table 4) and the corresponding lower potential U_s (Table 6) for electrons indicate that they are less efficient at depositing charge on the capillary surface, and the resulting charge patches may not produce a sufficient Coulomb field to guide subsequent incoming electrons. Therefore only a fraction of the incoming or primary electrons undergo elastic scattering with the deposited charge patches and are guided in a fashion similar to positive ions [37], whereas the majority of the incoming electrons suffer one or more collisions within the capillaries before being transmitted or lost inside the foil [92]. These collisions include both elastic and inelastic scattering of electrons within the capillaries [93—98], and, consequently, the transmitted electrons can have energies ranging from 0 to the full energy $E_{prim.}$ of the primary electron beam [93—99].

The transmitted electrons can be divided into two groups: (1) secondary electrons with energies from 0 to 50 eV and (2) inelastically backscattered and elastically scattered electrons with energies from 50 to $E_{prim.}$ [93, 95, 96, 99]. The total transmitted electron yield (σ) [93, 96, 98, 99] can be written as $\sigma = \int_0^{E_{prim}} J(E)dE = \int_0^{50} J(E)dE + \int_{50}^{E_{prim}} J(E)dE \equiv \delta + \eta$. Here, *J(E)* is the energy dependent distribution of electrons, or current density, a basic quantity for the description of emitted electrons, δ = (number of secondary electrons)/(number of primary electrons) is the secondary electron yield, and η = (number of reflected electrons)/(number of primary electrons) is the backscattering coefficient [96, 99]. The various scatterings of primary electrons with the surface and bulk of the material causing excitation and ionization of atoms or molecules and plasmon decay contribute to the generation of secondary electrons [93—99]. Secondary electrons are not only produced by the primary electrons but also by reflected electrons [95, 96, 99]. Only secondary electrons produced near the surface can reach and escape from the surface [93—99]. It should be noted that although the values of δ, η, and σ are not determined in the present measurements these are the important parameters in the context of interactions of high energy electron beams with insulators [93—98].

The secondary, inelastically backscattered, and elastically scattered electrons undergo the same scattering processes as those of the incident primary electron beam [93—99]. Thus, it is likely that most of the electrons have undergone several collisions within the capillaries before being transmitted with energies lower than the primary electron energy or before being lost within the foil [91, 96—98]. The various inelastic processes such as excitation and/or ionization of atoms or molecules associated with

electron transmission are likely the cause of the lower transmitted intensities of electrons than for ions.

Recent Monte Carlo simulations [65] of electrons interacting with an amorphous surface of Al_2O_3 at grazing incidence show evidence for inelastic scattering in contrast to results for the scattering of highly charged ions on a surface [1], supporting the conclusion that electron guiding through nanocapillaries is a different process than ion guiding. It was also predicted [65] that transmission of electrons through the capillaries can be achieved even without charge-up the inner walls of the capillaries. Therefore, the values of U_s in Table 6 for the elastically scattered electrons can be considered as the upper limits for the guiding of the electrons [65, 92].

Based on the present results, a scenario of electron guiding through an insulating nanocapillary can be envisioned as shown in Figure 35. A small fraction of the electron beam entering the capillary at an angle ψ is guided through the capillary due to deflection by the deposited charge in a fashion similar to positive ions [37] (see Figure 1). However, the majority of electrons interact with atoms at or just below the surface of the capillary due to the insufficient deposition of charges on the surface and therefore undergo elastic and inelastic scattering processes. Due to the Columbic attraction of the ion core of the atom they form jets of electrons moving generally in the forward direction as shown by i, ii, and iii in Figures 35i-35iii. A fraction of the electrons is therefore transmitted through the capillary with energies equal to or lesser than the energy of the incident electron beam (Fig. 35i), whereas a larger fraction (Figures 35ii-35iii) is lost inside the capillary due to various inelastic processes. The present measurements for 500 and 1000 eV electrons and comparison with results for

slow HCIs [37], support the conclusion that the transmission and guiding of electrons through nanocapillaries is quantitatively and qualitatively different than ion guiding.

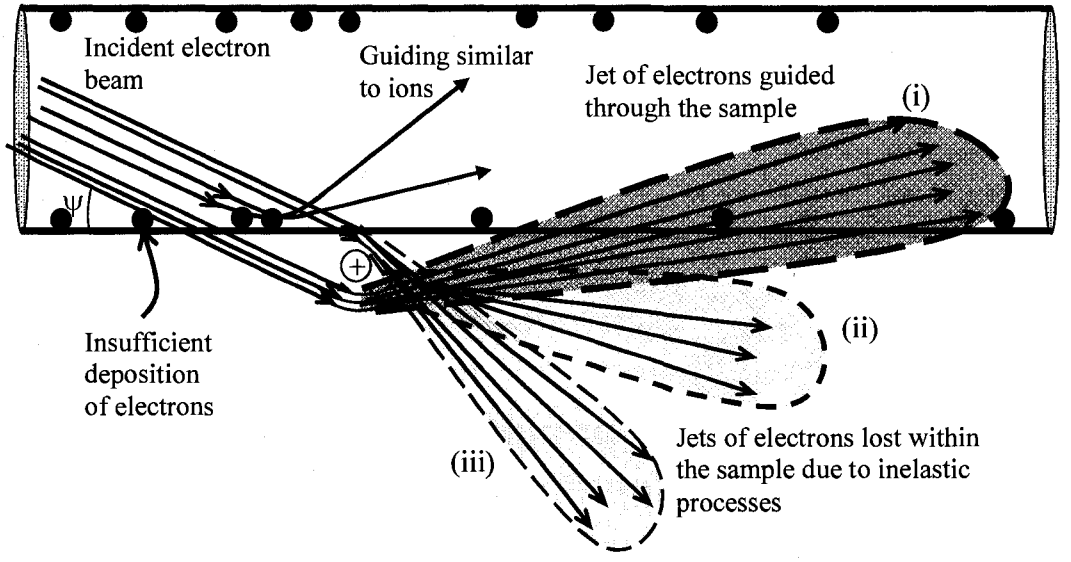

Figure 35. Scenario for electron transmission through an insulating nanocapillary.

Inelastic Processes Occurring During Electron Beam Bombardment of PET

The various inelastic processes that can occur when a PET polymer is bombarded by high energy electron beams are shown schematically in Figure 36 [86, 88, 100–105]. When the polymer is irradiated by a high energy (500 and 1000 eV) electron beam, inelastic processes can occur since the energy of the incident electron beam is higher than the valence shell and K-shell ionization energies of the carbon, oxygen, and hydrogen atoms that make up the sample, as well as the covalent bonding energies between the elements of the PET sample [86, 88, 100–103]. For example, the incident electron beam can excite or ionize C and O atoms leading to Auger processes [86, 88, 100]. Also, the beam could cause cleavage or rearrangement (e.g., formation of C = C bonds), or stretching (C – H stretching in CH_2 groups) or breaking

of the C – C or C – O or C = O or CH or C – O – C bonds, and could even affect the most stable benzene ring [88, 100, 104, 105].

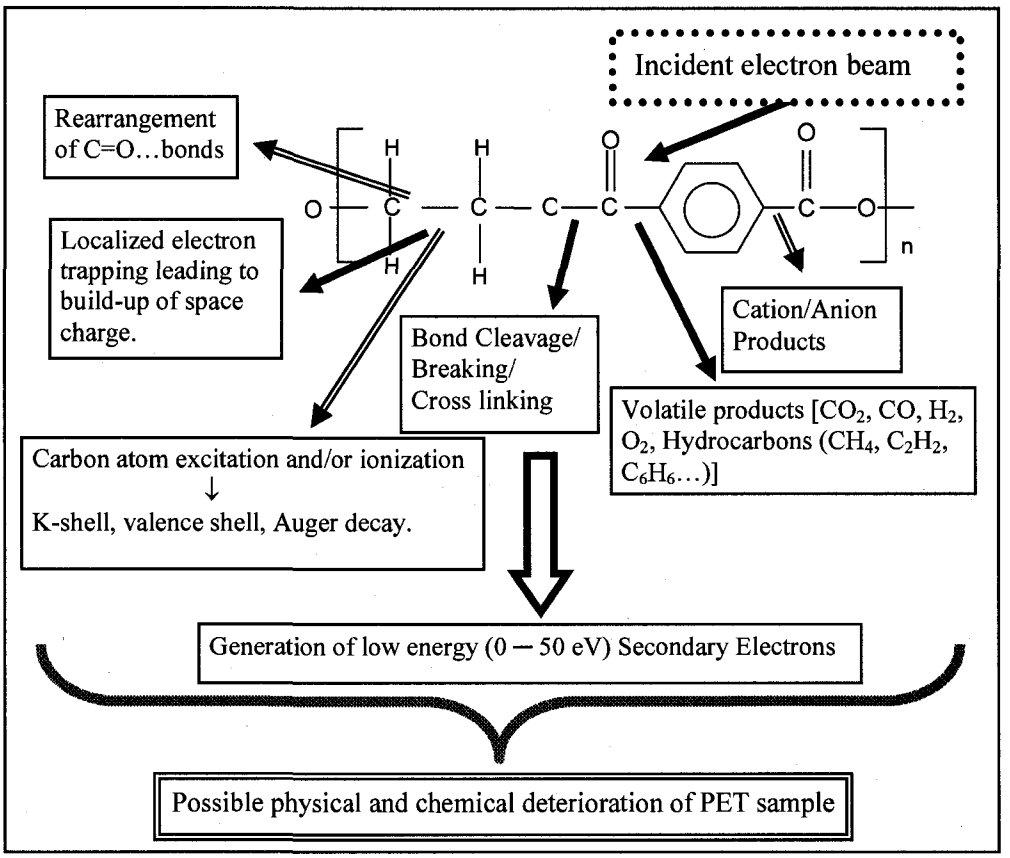

Figure 36. Electron beam irradiation of PET polymer.

As a result various volatile products [e.g., CO_2, CO, O_2, H_2 and hydrocarbons (CH_4, C_2H_2, C_6H_6, etc.,)] and cations/anions could be produced [100, 101, 104, 105]. The incident electron beam can locally heat up the interaction area, thereby ejecting secondary electrons from the surface, which in turn, increases the conductivity exponentially, leading to thermal breakdown of the polymer [88, 100]. The incoming electrons can also be trapped locally, thus creating a space charge [88, 100]. However, a survey of the literature reveals that the dynamics of the fundamental mechanism governing the scattering of electrons with insulators, unlike charged particle

interactions with metals [99, 106], has not been extensively studied due to the difficulties associated with charge build-up on the insulator surfaces.

16 MeV O^{5+} Ions Through PET

The same PET nanocapillary foil of length (L) 10 μm and diameter (D) 200 nm (aspect ratio, $\xi = L/D = 50$) was used to study the transmission of fast 16 MeV O^{5+} ions and its interactions with the capillary walls. The spectra of transmitted ions show that O^{5+} ions undergo significant energy losses and charge exchanges within the foil during the course of transmission. The results further support the deterioration of the sample.

The measurements were performed at Western Michigan University using the 6 MV tandem Van de Graaff accelerator. The ion beam was collimated to diameter of about 1.5 mm before it struck the sample. The sample was mounted on the goniometer. The goniometer assembly and operation were identical to the electron measurements (see Figure 2). The pressure in the chamber was ~ 10^{-6} Torr. Different charge states of the transmitted oxygen ions were separated magnetically and then counted using a silicon surface-barrier detector (SBD) that was moved along the radius of the analyzed ions as indicated in Figure 37. The counts on the detector were normalized to the beam current incident on the sample.

Figure 38 shows the transmitted ion spectra of 16 MeV O^{5+} ions incident on the PET foil for four angular positions of the SBD detector: at the positions of the (a) O^{5+}, (b) O^{6+}, (c) O^{7+}, and (d) O^{8+} charge states. No evidence of the transmitted O^{4+} charge state was found. The peaks near 15 MeV in Figure 38 correspond to the different charge states of elastically scattered oxygen ions. From kinematic calculations the peaks occurring near 5 MeV are attributed to recoiling gold ions coming either from the gold coated back surface of the capillaries or from inside of

the capillaries at the exit (the sample surfaces were coated with gold deposited at an angle of 45°), resulting from bombardment by the incident oxygen ion beam. The determination of the different charge states of the gold ions are given below:

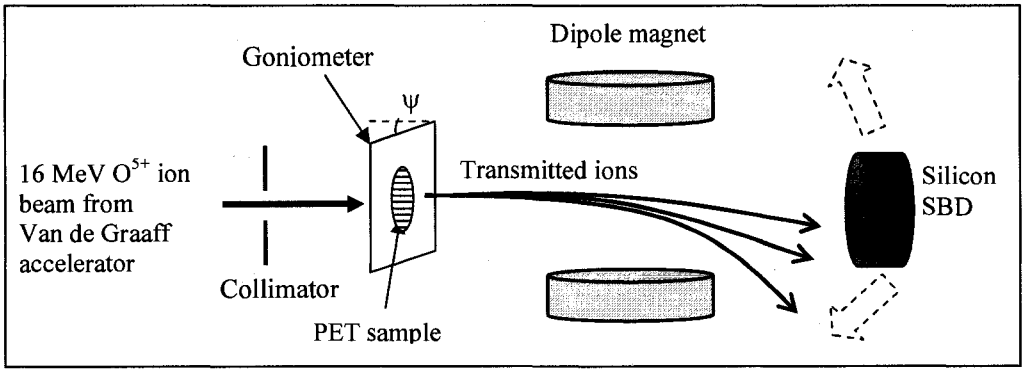

Figure 37. Schematic of the apparatus for measuring ion transmission.

Since the motion of a charged particle in a uniform magnetic field is circular, therefore, using the Lorentz force law we can write [107],

$$qvB = \frac{mv^2}{r}, \qquad 12$$

where q is the charge state of the ion, v is its velocity, B is the magnetic field, m is its mass, and r is the radius of the circle. From Equation 12 the magnetic field B can be written as,

$$B^2 = \frac{2mE}{q^2 r^2}, \qquad 13$$

where $E = \frac{1}{2}mv^2$ is the energy of the ion.

Therefore, for the same B and r for gold (Au) and oxygen (O) ions,

$$B_{Au}^2 = B_O^2$$

$$\Rightarrow \frac{2m_{Au}E_{Au}}{q_{Au}{}^2 r^2} = \frac{2m_O E_O}{q_O{}^2 r^2} \Rightarrow \frac{m_{Au}E_{Au}}{q_{Au}{}^2} = \frac{m_O E_O}{q_O{}^2} \qquad 14$$

For q_O = 6+, we have

$$\frac{197\times 5}{q_{Au}^2} = \frac{16\times 16}{6^2}$$

$$q_{Au} = 11 \Rightarrow \text{charge state } 11+ \text{ of gold ions.}$$

Using Equation 14, other charge states of gold ions are calculated as indicated in the Figure 38.

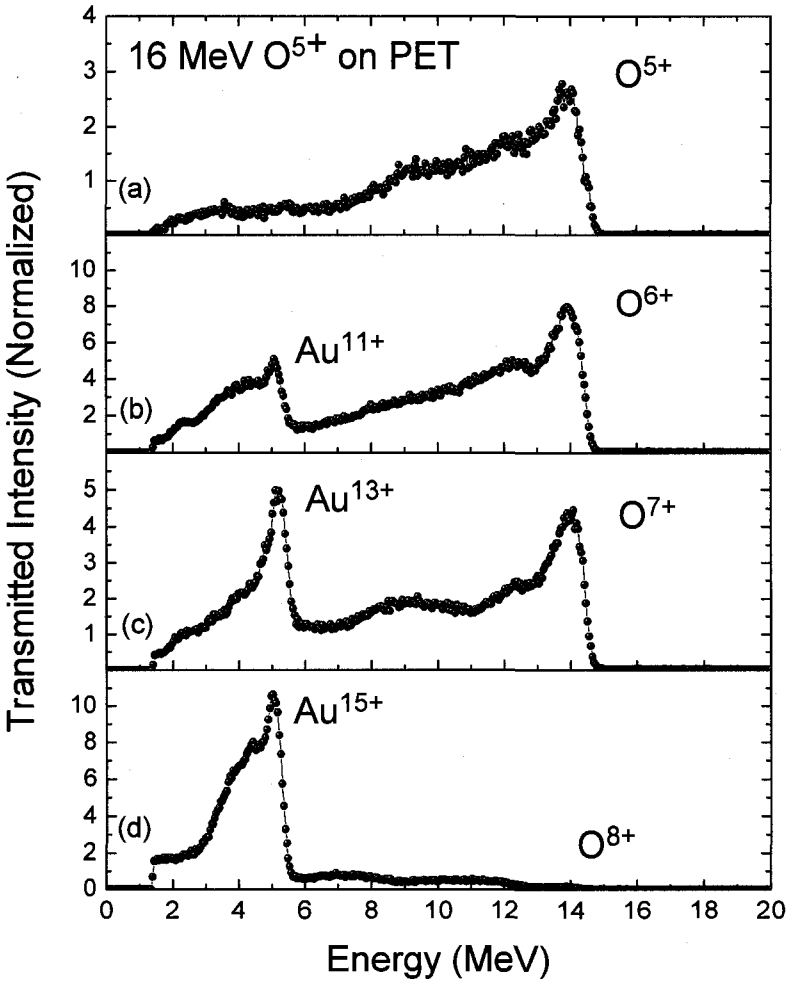

Figure 38. Spectra for 16 MeV O^{5+} ions transmitted through the PET sample.

The peaks occurring below 5 MeV can be due to the carbon ions. Figure 39 shows the angular distributions of the oxygen ions as a function of different detector position (angle). The transmitted intensity of the oxygen ions decreases with increasing tilt angle ψ as can be seen from Figure 39.

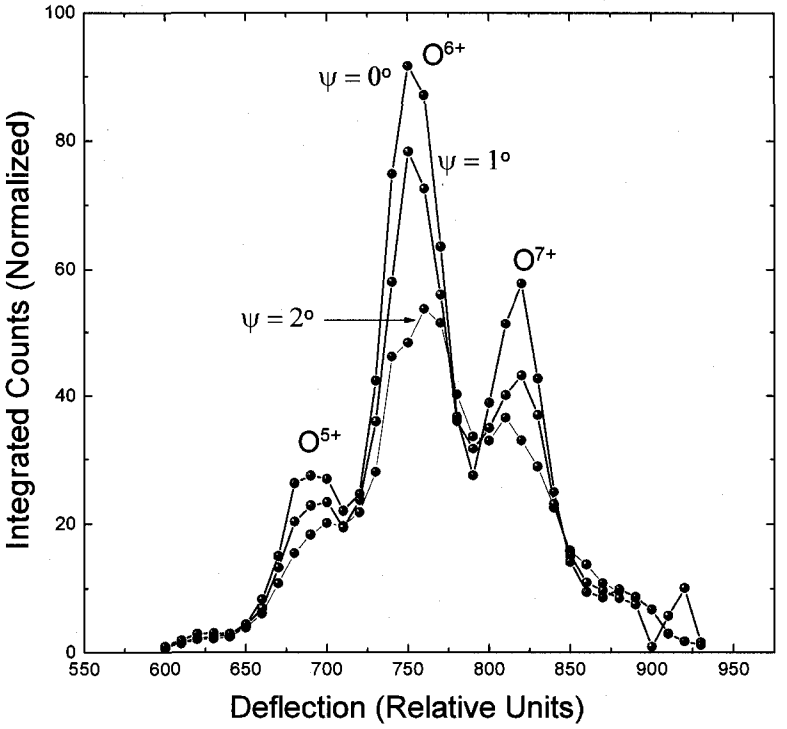

Figure 39. Angular distributions of the transmitted ion intensities for three different tilt angles $\psi = 0^{\circ}$, 1°, and 2°.

The appearance of charge changed oxygen ions, as well as gold and possibly carbon ions, as well as the observed energy loss in the transmitted spectra (Figure 38) suggest that O^{5+} ions have undergone close interactions with the capillary walls. The origin of carbon ions in the transmitted spectra is uncertain but is speculated to be from the hydrocarbons already deposited on the sample during the measurements for electron guiding as mentioned above or from the sample itself [104, 105]. Therefore, the energy losses and different charge states associated with the spectra of transmitted

oxygen ions through the PET sample are not only consistent with the hypothesis of the deterioration of the sample, but the fast ions may also further degrade the sample [108–110].

CHAPTER VI

CONCLUSIONS

The transmission and guiding of fast (500 and 1000 eV) electrons through insulating polyethylene terephthalate (PET or Mylar) nanocapillaries of length 10 μm and diameter 200 nm (aspect ratio 50) has been investigated and compared with the results for slow highly charged ions (HCIs). The measurements focused on the dependence of the transmission and guiding on the incident electron energy and foil tilt angle ψ. The angular distributions of the transmitted electrons clearly demonstrate that electrons are guided through the sample. The guiding has been found to depend on the foil tilt angle ψ and the incident energy, decreasing with increasing ψ and incident electron energy as already observed for slow HCIs.

Unlike positive ions and somewhat lower energy (200 — 350 eV) electrons, the transmitted spectra of 500 and 1000 eV electrons exhibit significant energy losses for which the fraction of electrons losing energy increases with foil tilt angle ψ and incident electron energy. The energy losses indicate that electrons suffer one or more close collisions inside the capillaries before being transmitted or lost within the foil. Despite considerable energy losses, both the inelastically and the elastically scattered electrons are observed to be guided through the sample.

The *characteristic guiding angle* ψ_c, which is a measure of the guiding ability of the capillaries, was calculated for both the elastically and inelastically scattered electrons through the sample and was found to be much lower than for positive ions of the same energy-to-charge ratio. This indicates that electron guiding falls off faster than for positive ions. Furthermore, the value of ψ_c for the elastic contributions is smaller than for the inelastic contributions. There is evidence that ψ_c for electrons

may also follow a scaling law dependent on the energy-to-charge ratio similar to that previously observed for slow HCIs, but this relationship needs further investigation.

It has been suggested that close collisions of electrons with the capillary walls, giving rise to excitation and ionization of atoms or molecules, are the likely causes for the observed lower transmission of electrons compared to positive ions. Comparative studies of the present measurements for electrons with results for slow positive ions indicate that the guiding mechanism for electrons is quantitatively and qualitatively different process than for slow highly charged ions.

In the initial measurements, the observed energy losses associated with the transmitted electron spectra were not anticipated as no evidence of energy losses has been found for slow HCIs until now. Therefore, the spectra taken were incomplete and did not cover the entire energy loss region. Hence, the measurements were later repeated at 500 eV using the same PET sample, this time covering the entire range of electron energy loss. The later measurements reproduced the essential transmission and energy loss features of the earlier measurements. In addition, a large reduction in the magnitude of the transmitted intensities was observed compared to the earlier measurements. This reduction was attributed to deterioration of the PET sample during the course of the earlier measurements. Possible causes were considered such as physical and chemical changes to the surface or capillary properties due to the intense electron bombardment of the sample.

The same PET sample was used to study the transmission of fast 16 MeV O^{5+} ions. The transmitted spectra indicate that O^{5+} ions undergo significant energy losses and charge exchange within the sample while being transmitted. Moreover, the appearance of gold and apparently carbon ions in the transmitted spectra support the hypothesis of deterioration of the sample.

A more detailed and systematic investigation of the underlying mechanisms responsible for electron guiding through insulating nanocapillaries and sample deterioration remains for future work.

BIBLIOGRAPHY

1. A. Arnau, F. Aumayr, P.M. Echenique, M. Grether, W. Heiland, J. Limburg, R. Morgenstern, P. Roncin, S. Schippers, R. Schuch, N. Stolterfoht, P. Varga, T.J.M. Zouros, and HP. Winter, *Interaction of slow multicharged ions with solid surfaces*, Surf. Sci. Rep. **27**, 113 (1997).

2. J. Burgdörfer, P. Lerner, and F.W. Meyer, *Above-surface neutralization of highly charged ions: The classical over-the-barrier model*, Phys. Rev. A **44**, 5674 (1991).

3. J. Burgdörfer, Chapter 11. *Atomic Collisions with Surfaces* in C.D. Lin (Ed.), Review of Fundamental Processes and Applications of Atoms and Ions, World Scientific (1993).

4. T. Schenkel, A.V. Hamza, A.V. Barnes, and D.H. Schneider, *Interaction of slow, very highly charged ions with surfaces*, Prog. Surf. Sci. **61**, 23 (1999).

5. H. Winter, *Hollow Atom Spectroscopy*, Phys. Scr. **T72**, 18 (1997); *Scattering of atoms and ions from insulator surfaces*, Prog. Surf. Sci. **63**, 177 (2000); *Image charge effects in ion surface scattering*, J. Phys.: Condens. Matter **8**, 10149 (1996); *Collisions of atoms and ions with surfaces under grazing incidence*, Phys. Rep. **367**, 387 (2002).

6. Y. Yamazaki, S. Ninomiya, F. Koike, H. Masuda, T. Azuma, K. Komaki, K. Kuroki, and M. Sekiguchi, *Stabilized Hollow Atoms (Ions) Produced with Multiply Charged Ions Passed through Microcapillaries*, J. Phys. Soc. Jpn. **65**, 1199 (1996).

7. S. Ninomiya, Y. Yamazaki, F. Koike, H. Masuda, T. Azuma, K. Komaki, K. Kuroki, and M. Sekiguchi, *Stabilized Hollow Ions Extracted in Vacuum*, Phys. Rev. Lett. **78**, 4557 (1997); S. Ninomiya, Y. Yamazaki, T. Azuma, K. Komaki, F. Koike, H. Masuda, K. Kuroki, and M. Sekiguchi, *Stabilized Hollow Atoms (Ions) Produced with Slow Multiply Charged Ions Passed Through Metallic Microcapillaries*, Phys. Scr. T**73**, 316 (1997).

8. Y. Yamazaki, *Beam capillary spectroscopy*, Int. J. Mass Spectrom. **192**, 437 (1999); *A microcapillary target as a metastable hollow ion source*, Nucl. Instrum. Methods Phys. Res. B **193**, 516 (2002).

9. J. Limburg, *Hollow-Atom Probing of Surfaces*, Phys. Scr. **T73**, 298 (1997).

10. E.S. Parilis, *Radiation effects under multiply charged ion impacts*, Nucl. Instrum. Methods Phys. Res. B **116**, 478 (1996); *Coulomb Explosion Sputtering, Crater and Blister formation by HCI*, Phys. Scr. **T92**, 197 (2001).

11. F. Aumayr, J. Burgdörfer, G. Hayderer, P. Varga, and HP. Winter, *Evidence against the "Coulomb Explosion" Model for Desorption from Insulator Surfaces by Slow Highly Charged Ions*, Phys. Scr. **T80**, 240 (1999).

12. H. Winter and F. Aumayr, *Hollow atoms*, J. Phys. B **32**, R39 (1999); *Interaction of Slow HCI with Solid Surfaces: What Do We Know, What Should We Know?*, Phys. Scr. **T92**, 15 (2001).

13. J.D. Gillaspy, *Highly charged ions*, J. Phys. B **34**, R93 (2001).

14. Y. Yamazaki, *Production of Hollow Atoms (Ions) in HCI-Surface Collision*, Phys. Scr. **T73**, 293 (1997); Y. Yamazaki, Chapter 2. *Interaction of Slow Highly Charged Ions with Surfaces* in F.J. Currell (Ed.), The Physics of Multiply and Highly Charged Ions, Vol. 2, Kluwer Academic Publishers (2003).

15. N. Stolterfoht, Chapter 3. *Interaction of Hollow Atoms with Surfaces: Auger electron emission and plasmon excitation* in F.J. Currell (Ed.), The Physics of Multiply and Highly Charged Ions, Vol. 2, Kluwer Academic Publishers (2003).

16. F. Aumayr and HP. Winter, *Inelastic interactions of slow ions and atoms with surfaces*, Nucl. Instrum. Methods Phys. Res. B **233**, 111 (2005).

17. K. Tökési, L. Wirtz, C. Lemell, and J. Burgdörfer, *Charge-state evolution of highly charged ions transmitted through microcapillaries*, Phys. Rev. A **61**, 020901 (R) (2000); *Hollow-ion formation in microcapillaries, ibid.* **64**, 042902 (2001); *Angular distribution of highly charged ions transmitted through metallic microcapillaries*, J. Electron. Spectrosc. Relat. Phenom. **129**, 195 (2003).

18. C. Lemell, M. Alducin, J. Burgdörfer, J.I. Juaristi, K. Schiessl, B. Solleder, and K. Tökési, *Interaction of slow multicharged ions with surfaces*, Radiat. Phys. Chem. **76**, 412 (2007).

19. Y. Yamazaki, *Interaction of slow highly-charged ions with metals and insulators*, Nucl. Instrum. Methods Phys. Res. B **258**, 139 (2007).

20. Y. Kanai, Y. Nakai, Y. Iwai, K. Nishio, H. Masuda, and Y. Yamazaki, *Auger electrons emitted form nitrogen ions passing through a metallic nanocapillary*, J. Phys.: Conf. Ser. **58**, 335 (2007).

21. H. Watanabe, T. Abe, Y. Fujita, J. Sun, S. Takahashi, M. Tona, N. Yoshiyasu, N. Nakamura, M. Sakurai, C. Yamada, and S. Ohtani, *X-ray emission in slow highly charged ion-surface collisions*, J. Phys.: Conf. Ser. **58**, 339 (2007).

22. S. Facsko, D. Kost, A. Keller, W. Möller, Z.D. Pešić, and N. Stolterfoht, *Interaction of highly charged ions with insulator surfaces*, Radiat. Phys. Chem. **76**, 387 (2007).

23. F. Aumayr and H. Winter, *Slow Highly Charged Ions – A New Tool For Surface Nanostructuring ?*, e-J. Surf. Sci. Nanotech. **1**, 171 (2003).

24. I.C. Gebeshuber, S. Cernusca, F. Aumayr, and H.P. Winter, *Nanoscopic surface modification by slow ion bombardment*, Int. J. Mass Spetrom. **229,** 27 (2003).

25. T. Schenkel, A. Persaud, S.J. Park, J. Nilsson, J. Bokor, J.A. Liddle, R. Keller, D.H. Schneider, D.W. Cheng, and D.E. Humphries, *Solid state quantum computer development in silicon with single ion implantation*, J. Appl. Phys. **94**, 7017 (2003).

26. T. Schenkel, I.W. Rangelow, R. Keller, S.J. Park, J. Nilsson, A. Persaud, V.R. Radmilovicv, P. Grabiec, D.H. Schneider, J.A. Liddle, and J. Boker, *Open questions in electronic sputtering of solids by slow highly charged ions with respect to applications in single ion implantation*, Nucl. Instrum. Methods Phys. Res. B **219-220**, 200 (2004).

27. *A Quantum Information Science and Technology Roadmap, Part 1: Quantum Computation*, 2004 (http://qist.lanl.gov/).

28. F. Watt, A.A. Bettiol, J.A. Van Kan, E.J. Teo, and M.B.H. Breese, *Ion beam lithography and nanofabrication: A Review*, Int. J. of Nanoscience **4**, 269 (2005).

29. S. Takahashi, M. Tona, K. Nagata, N. Yoshiyasu, N. Nakamura, M. Sakurai, C. Yamada, and S. Ohtani, *Observation of surface modification and secondary particle emission in HCI-surface interaction*, Nucl. Instrum. Methods Phys. Res. B **235**, 456 (2005).

30. J.D. Gillaspy, J.M. Pomeroy, A.C. Perrella, and H. Grube, *The potential of highly charged ions: possible future applications,* J. Phys.: Conf. Ser. **58**, 451 (2007).

31. E. Akcöltekin, T. Peters, R. Meyer, A. Duvenbeck, M. Klusmann, I. Monnet, H. Lebius, and M. Schleberger, *Creation of multiple nanodots by single ions*, Nature Nanotech. **2**, 290 (2007).

32. C. Lemell, A.S. El-Said, W. Meissl, I.C. Gebeshuber, C. Trautmann, M. Toulemonde, J. Burgdörfer, and F. Aumayr, *On the nano-hillock formation induced by slow highly charged ions on insulator surfaces*, Solid-State Electron. **51**, 1398 (2007).

33. M. Tona, H. Watanabe, S. Takahashi, Y. Fujita, T. Abe, S. Jian, N. Nakamura, N. Yoshiyasu, C. Yamada, , M. Sakurai, and S. Ohtani, *Observation of HCI-induced nanostructures with a scanning probe microscope*, J. Phys.: Conf. Ser. **58**, 331 (2007).

34. F. Aumayr, *Highly charged ion-induced nanostructures on surfaces*, page-41, K. Póra *et al.* (Ed.), Book of Abstracts, 4th Conference on Elementary Processes in Atomic Systems (CEPAS), Babeş-Bolyai University, Cluj-Napoca, Romania, June 18-20, 2008; *Nanostructures produced by slow highly charged ions*, page-49, H. Lebius *et al.* (Ed.), Book of Abstracts, 17th International Workshop on Inelastic Ion-Surface Collisions (11SC-17), Porquerolles, France, September 21-26, 2008.

35. A.S. El-Said, W. Meissl, M.C. Simon, J.R.C. López-Urrutia, I.C. Gebeshuber, J. Laimer, H.P. Winter, J. Ullrich, and F. Aumayr, *Creation of surface nanostructures by irradiation with slow, highly charged ions,* Radiat. Eff. Defects Solids **162**, 467 (2007); A.S. El-Said, W. Meissl, M.C. Simon, J.R.C. López-Urrutia, I.C. Gebeshuber, M. Lang, H.P. Winter, J. Ullrich, and F. Aumayr, *Surface nanostructures induced by slow highly charged ions on CaF_2 single crystals*, Nucl. Instrum. Methods Phys. Res. B **256,** 346 (2007); A.S. El-Said, R. Heller, W. Meissl, R. Ritter, S. Facsko, C. Lemell, B. Solleder, I.C. Gebeshuber, G. Betz, M. Toulemonde, W. Möller, J. Burgdörfer, and F. Aumayr, *Creation of Nanohillocks on CaF_2 Surfaces by Single Slow Highly Charged Ions,* Phys. Rev. Lett. **100**, 237601 (2008).

36. F. Aumayr, A.S. El-Said, and W. Meissl, *Nano-sized surface modifications induced by the impact of slow highly charged ions-A first review*, Nucl. Instrum. Methods Phys. Res. B **266,** 2729 (2008).

37. N. Stolterfoht, J.-H. Bremer, V. Hoffmann, R. Hellhammer, D. Fink, A. Petrov, and B. Sulik, *Transmission of 3 keV Ne^{7+} Ions through Nanocapillaries Etched in Polymer Foils: Evidence for Capillary Guiding*, Phys. Rev. Lett. **88**, 133201 (2002).

38. N. Stolterfoht, V. Hoffmann, R. Hellhammer, Z.D. Pešić, D. Fink, A. Petrov, and B. Sulik, *Guided transmission of 3 keV Ne^{7+} ions through nanocapillaries etched in a PET polymer*, Nucl. Instrum. Methods Phys. Res. B **203**, 246 (2003).

39. N. Stolterfoht, R. Hellhammer, Z.D. Pešić, V. Hoffmann, J. Bundesmann, A. Petrov, D. Fink, B. Sulik, M. Shah, K. Dunn, J. Pedregosa, and R.W. McCullough, *Time evolution of ion guiding through nanocapillaries in a PET polymer*, Nucl. Instrum. Methods Phys. Res. B **225**, 169 (2004).

40. N. Stolterfoht, R. Hellhammer, Z.D. Pešić, V. Hoffmann, J. Bundesmann, A. Petrov, D. Fink, and B. Sulik, *Guided transmission of Ne^{7+} ions through nanocapillaries in PET: dependence on the tilt angle*, Vacuum **73**, 31 (2004).

41. R. Hellhammer, P. Sobocinski, Z.D. Pešić, J. Bundesmann, D. Fink, and N. Stolterfoht, *Interaction of slow highly charged ions with the inner surface of nanocapillaries*, Nucl. Instrum. Methods Phys. Res. B **232**, 235 (2005).

42. R. Hellhammer, Z.D. Pešić, P. Sobocinski, D. Fink, J. Bundesmann, and N. Stolterfoht, *Guided transmission of highly charged ions through nanocapillaries in PET: Study of the energy dependence*, Nucl. Instrum. Methods Phys. Res. B **233**, 213 (2005).

43. Gy. Víkor, R.T. Rajendra Kumar, Z.D. Pešić, N. Stolterfoht, and R. Schuch, *Guiding of slow highly charged ions by nanocapillaries in PET*, Nucl. Instrum. Methods Phys. Res. B **233**, 218 (2005).

44. N. Stolterfoht, R. Hellhammer, P. Sobocinski, Z.D. Pešić, J. Bundesmann, B. Sulik, M.B. Shah, K. Dunn, J. Pedregosa, and R.W. McCullough, *Guiding of slow neon and molecular hydrogen ions through nanocapillaries in PET*, Nucl. Instrum. Methods Phys. Res. B **235**, 460 (2005).

45. N. Stolterfoht, R. Hellhammer, Z.D. Pešić, V. Hoffmann, J. Bundesmann, A. Petrov, D. Fink, and B. Sulik, *Guiding of slow Ne^{7+} ions through nanocapillaries in a PET polymer: dependence on the capillary diameter*, Surf. Coat. Technol. **196**, 389 (2005).

46. R. Hellhammer, J. Bundesmann, D. Fink, and N. Stolterfoht, *Scaling laws for guiding of highly charged ions through nanocapillaries in insulating PET*, Nucl. Instrum. Methods Phys. Res. B **258**, 159 (2007).

47. R. Hellhammer, D. Fink, and N. Stolterfoht, *Guiding of highly charged ions through nanocapillaries in PET: Dependence on the projectile energy and charge*, Nucl. Instrum. Methods Phys. Res. B **261**, 149 (2007).

48. S. Mátéfi-Tempfli, M. Mátéfi-Tempfli, L. Piraux, Z. Juhász, S. Biri, É. Fekete, I. Iván, F. Gáll, B. Sulik, Gy. Víkor, J. Pálinkás, and N. Stolterfoht, *Guided transmission of slow Ne^{6+} ions through the nanochannels of highly ordered anodic alumina*, Nanotechnology **17**, 3915 (2006).

49. Y. Kanai, M. Hoshino, T. Kambara, T. Ikeda, R. Hellhammer, N. Stolterfoht, and Y. Yamazaki, *Two-dimensional images of transmitted slow neon ions guided by nanocapillaries in polymer foils*, Nucl. Instrum. Methods Phys. Res. B **258**, 155 (2007).

50. M. Fürsatz, W. Meissl, S. Pleschko, I.C. Gebeshuber, N. Stolterfoht, HP. Winter, and F. Aumayr, *Charging and discharging of nano-capillaries during ion guiding of multiply charged projectiles*, J. Phys.: Conf. Ser. **58**, 319 (2007).

51. N. Stolterfoht, R. Hellhammer, J. Bundesmann, and D. Fink, *Guiding of slow highly charged ions through insulating nanocapillaries in PET polymers*, Radiat. Eff. Defects Solids **162**, 515 (2007).

52. N. Stolterfoht, R. Hellhammer, J. Bundesmann, D. Fink, Y. Kanai, M. Hoshino, T. Kambara, T. Ikeda, and Y. Yamazaki, *Guiding of slow Ne^{7+} ions through nanocapillaries in insulating polyethylene terephthalate: Incident current dependence*, Phys. Rev. A **76**, 022712 (2007).

53. N. Stolterfoht, R. Hellhammer, J. Bundesmann, and D. Fink, *Scaling laws for guiding of highly charged ions through nanocapillaries in an insulating polymer*, Phys. Rev. A **77**, 032905 (2008).

54. M.B. Sahana, P. Skog, Gy. Víkor, R.T. Rajendra Kumar, and R. Schuch, *Guiding of highly charged ions by highly ordered SiO_2 nanocapillaries*, Phys. Rev. A **73**, 040901(R) (2006); R.T. Rajendra Kumar, X. Badel, G. Víkor, J. Linnros, and R. Schuch, *Fabrication of silicon dioxide nanocapillary arrays for guiding highly charged ions*, Nanotechnology **16**, 1697 (2005).

55. P. Skog, I.L. Soroka, A. Johansson, and R. Schuch, *Guiding of highly charged ions through Al_2O_3 nano-capillaries*, Nucl. Instrum. Methods Phys. Res. B **258**, 145 (2007).

56. H.F. Krause, C.R. Vane, and F.W. Meyer, *Ions transmitted through an anodic nanocapillary array*, Phys. Rev. A **75**, 042901 (2007); H.F. Krause, C.R. Vane, F.W. Meyer, and H.M. Christen, *Angular distribution of ions transmitted by an anodic nanocapillary array*, J. Phys.: Conf. Ser. **58,** 323 (2007).

57. K. Schiessl, W. Palfinger, K. Tőkési, H. Nowotny, C. Lemell, and J. Burgdörfer, *Simulation of guiding of multiply charged projectiles through insulating capillaries*, Phys. Rev. A **72**, 062902 (2005); *Simulation of ion guiding through insulating capillaries: Effects of inter-capillary interaction*, Nucl. Instrum. Methods Phys. Res. B **258**, 150 (2007); *Simulation of guiding of multiply charged projectiles through insulating capillaries*, arXiv: physics/0508165v1 [physics.atom-ph] 2005; K. Schiessl, W. Palfinger, C. Lemell, and J. Burgdorfer, *Simulation of guiding of highly charged projectiles through insulating nanocaplillaries*, Nucl. Instrum. Methods Phys. Res. B **232**, 228 (2005).

58. C. Lemell, K. Schiessl, H. Nowotny, and J. Burgdörfer, *Simulation of heavy-ion guiding in insulators*, Nucl. Instrum. Methods Phys. Res. B **256**, 66 (2007); C. Lemell, M. Alducin, J. Burgdörfer, J.I. Juaristi, K. Schiessl, B. Solleder, and K. Tökési, *Interaction of slow multicharged ions with surfaces,* Radiat. Phys. Chem. **76**, 412 (2007).

59. A.R. Milosavljević, Gy. Víkor. Z.D. Pešić, P. Kolarž, D. Šević, B.P. Marinković, S.Mátéfi-Tempfli, M. Mátéfi-Tempfli, and L. Piraux, *Guiding of low-energy electrons by highly ordered Al_2O_3 nanocapillaries*, Phys. Rev. A **75**, 030901(R) (2007).

60. T. Nebiki, T. Yamamoto, T. Narusawa, M.B.H. Breese, E.J. Teo, and F. Watt, *Focusing of MeV ion beams by means of tapered glass capillary optics*, J. Vac. Sci. Technol. A **21**, 1671 (2003).

61. T. Nebiki, M. H. Kabir, and T. Narusawa, *In-air PIXE analysis by means of glass capillary optics*, Nucl. Instrum. Methods Phys. Res. B **249**, 226 (2006).

62. T. Ikeda, Y. Kanai, T.M. Kojima, Y. Iwai, T. Kambara, Y. Yamazaki, M. Hoshino, T. Nebiki, and T. Narusawa, *Production of a microbeam of slow highly charged ions with a tapered glass capillary*, Appl. Phys. Lett. **89,** 163502 (2006).

63. T. Ikeda, T.M. Kojima, Y. Iwai, Y. Kanai, T. Kambara, T. Nebiki, T. Narusawa, and Y. Yamazaki, *Production of a nm sized slow HCI beam with a guiding effect*, J. Phys.: Conf. Ser. **58**, 68 (2007); T. Ikeda, Y. Kanai, T.M. Kojima, Y. Iwai, Y. Kanazawa, M. Hoshino, T. Kobayashi, G.P. Pokhil, and Y. Yamazaki, *Focusing of charged particle beams with various glass-made optics*, J. Phys.: Conf. Ser. **88**, 012031 (2007).

64. T.M. Kojima, D. Tomono, T. Ikeda, K. Ishida, Y. Iwai, M. Iwasaki, Y. Matsuda, T. matsuzaki, and Y. Yamazaki, *Density Enhancement of Muon Beams with Tapered Glass Tubes*, J. Phys. Soc. Jpn. **76**, 093501 (2007).

65. B. Stix, S. Pleschko, K. Schiessl, K. Tőkesi, C. Lemell, B. Solleder, and J. Burgdörfer, *Guiding of Charged Particles Through Insulating Nanocapillaries: Comparison Between Ions and Electrons*, Abstracts, MO 128, XXV International Conference on Photonic, Electronic, and Atomic Collisions, Freiburg, Germany, July 2007.

66. Y. Iwai, T. Ikeda, T.M. Kojima, Y. Yamazaki, K. Maeshima, N. Imamoto, T. Kobayashi, T. Nebiki, T. Narusawa, and G.P. Pokhil, *Ion irradiation in liquid of μm^3 region for cell surgery*, App. Phys. Lett. **92**, 023509 (2008).

67. R. Schuch, A. Johansson, R.T. R. Kumar, M.B. Sahana, P. Skog, I.L. Soroka, Gy. Vikor, and H.Q. Zhang, *Guiding of highly charged ions through insulating nanocapillaries*, Can. J. Phys. **86**, 327 (2008).

68. P. Skog, H.Q. Zhang, and R. Schuch, *Evidence of Sequentially Formed Charge Patches Guiding Ions through Nanocapillaries*, Phy. Rev. Lett. **101**, 223202 (2008).

69. C. Xi-Meng, X. Fa-Yuan, Q. Xi-Yu, S. Jian-Xiong, C. Ying, S. Guang-Zhi, W. Jun, C. Yi-Feng, L. Hui-Ping, Y. Yong-Zhi, L. Feng-Jun, W. Xing-An, X. Jun-Kui, and Z. Chun-Lin, *Guiding of 60 keV O^{6+} Ions through Nanocapillaries in an Uncoated Al_2O_3 Membrane*, Chin. Phys. Lett. **25**, 4348 (2008).

70. A. Cassimi, T. Muranaka, L. Maunoury, H. Lebius, B. Manil, B.A. Huber, T. Ikeda, Y. Kanai, T.M. Kojima, Y. Iwai, T. Kambara, Y. Yamazaki, T. Nebiki, and T. Narusawa, *Multiply-charged ion nanobeams,* Int. J. Nanotechnol. **5**, 809 (2008).

71. N. Stolterfoht, R. Hellhammer, B. Sulik, Z. Juhász, H.M. Dang, and R. Hokestra, *Ion guiding through nanocapillaries in PET polymers with variable diameter*, H. Lebius *et al.* (Ed.), Book of Abstracts, page-40, 17th International Workshop on Inelastic Ion-Surface Collision (IISC-17), Porquerolles, France, September 21 – 26, 2008.

72. C. Xi-Meng, W. Jun, W. Xing-An, S. Guang-Zhi, C. Yi-Feng, X. Fa-Yuan, S. Jian-Xiong, C. Ying, D. Bao-Wei, X. Jun-Kui, L. Feng-Jun, Y. Yong-Zhi, Z. Chun-

Lin, and Q. Xi-Yu, *Interaction of O^{3+} Ions with Al_2O_3 Nanocapillaries*, Chin. Phys. Lett. **25**, 4255 (2008).

73. R.J. Bereczky, G. Kowarik, F. Aumayr, and K. Tőkési, *Transmission of 4.5 keV Ar^{9+} ions through a single glass macro-capillary*, Nucl. Instrum. Methods Phys. Res. B **267**, 317 (2009).

74. N. Stolterfoht, R. Hellhammer, J. Bundesmann, and D. Fink, *Density effects on the guided transmission of 3 keV Ne^{7+} ions through PET nanocapillaries*, Nucl. Instrum. Methods Phys. Res. B **267**, 226 (2009).

75. N. Stolterfoht, R. Hellhammer, D. Fink, B. Sulik, Z. Juhász, E. Bodewits, H.M. Dang, and R. Hokestra, *Time evolution of ion guiding through nanocapillaries in a PET polymer*, Nucl. Instrum. Methods Phys. Res. B **267**, 669 (2009).

76. Z. Juhász, B. Sulik, S. Biri, I. Iván, K. Tőkesi, É. Fekete, S. Mátéfi-Tempfli, M. Mátéfi-Tempfli, Gy. Víkor, E. Takács, and J. Pálinkás, *Ion guiding in alumina capillaries: MCP images of the transmitted ions*, Nucl. Instrum. Methods Phys. Res. B **267**, 321 (2009).

77. D.H. Li, Y.Y. Wang, Y.T. Zhao, G.Q. Xiao, D. Zhao, Z.F. Xu, and F.L. Li, *The influence of the charged back side on the transmission of highly charged ions through PC nanocapillaries*, Nucl. Instrum. Methods Phys. Res. B **267**, 469 (2009).

78. A. Cassimi, L. Maunoury, T. Muranaka, B. Huber, K.R. Dey, H. Lebius, D. Lelièvre, J.M. Ramillon, T. Been, T. Ikeda, Y. Kanai, T.M. Kojima, Y. Iwai, Y. Yamazaki, H. Khemliche, N. Bundaleski, and P. Roncin, *Imaging dynamic of charge-auto-organisation in glass capillaries*, Nucl. Instrum. Methods Phys. Res. B **267**, 674 (2009).

79. B.S. Dassanayake, R.J. Bereczky, S. Das, K. Tőkési, and J.A. Tanis, *Guiding of electrons through a single glass macrocapillary*, ATOMKI Annual Report, Debrecen, Hungary (2008) (submitted); B.S. Dassanayake, R.J. Bereczky, S. Das, K. Tőkési, and J.A. Tanis, *Energy dependence of electron transmission through a single glass capillary*, XXVIth ICPEAC, USA, July 22-28, 2009 (submitted).

80. N. Stolterfoht, R. Hellhammer, D. Fink, B. Sulik, Z. Juhász, E. Bodewits, H.M. Dang, and R. Hokestra, *Dynamic properties of ion guiding through nanocapillaries in an insulating polymer*, Phys. Rev. A **79**, 022901 (2009).

81. Y. Kanai, M. Hoshino, T. Kambara, T. Ikeda, R. Hellhammer, N. Stolterfoht, and Y. Yamazaki, *Dynamic features of ion guiding by nanocapillaries in an insulating polymer*, Phys. Rev. A **79**, 012711 (2009).

82. A.R. Milosavljević, J. Jureta, Gy. Víkor. Z.D. Pešić, D. Šević, , S.Mátéfi-Tempfli, M. Mátéfi-Tempfli, and B.P. Marinković, *Transmission of electrons through Al_2O_3 nanocapillaries in the energy range 2-120 eV*, Publ. Astron. Obs. Belgrade, No. 84, 189 (2008).

83. S. Rumega, *Control and Data Acquisition for an Electron Spectrometer System*, M. A. Thesis, Department of Physics, Western Michigan University (2000) (unpublished).

84. J.H. Moore, C.C. Davis, and M.A. Coplan, Chapter 5: *Charged-Particle Optics* of *Building Scientific Apparatus* in A Practical Guide to Design and Construction (Second Edition) (ISBN 0-201-13187-0), Addison – Wesley Publishing Company Inc.

85. *Channeltron Electron Multiplier Handbook for Mass Spectrometry Applications*, BURLE Electro-Optics Inc. (http://www.burle.com/cgi-bin/byteserver.pl/pdf/ChannelBook.pdf).

86. Chapters 1, 7, 9, and 10 in D. Fink (Ed.), Fundamentals of Ion-Irradiated Polymers, Springer-Verlag, Germany (ISBN 354004027) (2004).

87. D.R. Lide (Ed.), CRC Handbook of Chemistry and Physics, 87th edition, (2006-2007).

88. L.A. Dissado and J.C. Fothergill, Electrical Degradation and Breakdown in Polymers (IEE Materials and Devices Series), Peter Peregrinus for IEE, London (ISBN 0863411967) (1992).

89. R. Hellhammer, Helmholtz-Zentrum Berlin, *Private Communication.*

90. R.N. Bracewell, *The Fourier Transform and Its Applications* (3rd edition), M^{c} Graw Hill; H.J. Weaver, *Theory of Discrete and Continuous Fourier Analysis*, John Wiley & Sons.; H.D. Meikle, *A New Twist to Fourier Transforms*, Wiley-VCH.

91. F. Aumayr and H. Winter, Chapter 3. *Potential Electron Emission from Metal and Insulator Surfaces*, in H.P. Winter and J. Burgdörfer (Ed.), Slow Heavy-Particle

Induced Electron Emission from Solid Surfaces, Springer Tracts in Modern Physics, Vol. 225, Springer (ISSN electronic edition: 1615-0430) (2008).

92. N. Stolterfoht, Helmholtz-Zentrum Berlin, *Private Communication.*

93. K. Kanaya, S. Ono, and F. Ishigaki, *Secondary electron emission from insulators*, J. Phys. D **11**, 2425 (1978).

94. A. Jablonski, *Elastic Backscattering of Electrons from Surfaces*, Surf. Sci. **151**, 166 (1985).

95. Z.G. Song, C.K. Ong, and H. Gong, *Secondary and backscattered electron yields of polymer surface under electron beam irradiation*, Appl. Surf. Sci. **119**, 169 (1997).

96. H. Seiler, *Secondary electron emission in the scanning electron microscope*, J. Appl. Phys. **54**, R1 (1983).

97. M. Yasuda, T. Nobuo, and H. Kawata, *A Monte Carlo Calculation of Secondary Electron Emission from Organic Compounds*, Jpn. J. Appl. Phys. **43**, 4004 (2004).

98. R. Renoud, F. Mady, C. Attard, J. Bigarré, and J.-P. Ganachaud, *Secondary electron emission of an insulating target induced by a well-focused electron beam-Monte Carlo simulation study*, Phys. Stat. Sol. (a) **201**, 2119 (2004).

99. M. Rösler and W. Brauer, *Theory of Electron Emission from Nearly-Free-Electron Metals by Proton and Electron Bombardment* in G.Höhler (Ed.), Particle Induced Electron Emission I, Springer Tracts in Modern Physics, Vol. 122, Springer (ISBN 3-540-53431) (1991).

100. D.T. Turner, Chapter 8. *Polyethylene Terephthalate* in M. Dole (Ed.), The Radiation Chemistry of Macromolecules, Volume II, Academic Press, New York and London (1973).

101. L. Sanche, *Irradiation of organic and polymer films with low-energy electrons*, Nucl. Instrum. Methods Phys. Res. B **208**, 4 (2003).

102. C.K. Ong, Z.G. Song, and H. Gong, *Dynamics aspects of the charging behaviour of polymers under focused electron beam irradiation*, J. Phys.: Condes. Matter **9**, 9289 (1997).

103. H. Gong, Z.G. Song, and C.K. Ong, *Space-charge dynamics of polymethylmethacrlyate under electron beam irradiation*, J. Phys.: Condes. Matter **9**, 5027 (1997).

104. A. Chapiro, *Chemical Modifications in Irradiated Polymers*, Nucl. Instrum. Methods Phys. Res. B **32**, 111 (1988).

105. L. Calcagno, G. Compagnini, and G. Foti, *Structural modifications of polymer films by ion irradiation*, Nucl. Instrum. Methods Phys. Res. B **65**, 413 (1992).

106. M. Rösler, *Theory of particle-induced kinetic electron emission from simple metals: Comparative studies of different excitation and scattering mechanisms for Al, Mg, and Be*, Appl. Phys. A **61**, 595 (1995); *Comparative study of ion-induced kinetic electron emission from different nearly-free-electron metals*, Nucl. Instrum. Methods Phys. Res. B **115**, 278 (1996).

107. D.J. Griffiths, *Introduction to Electrodynamics* (3rd edition), Prentice-Hall of India Private Limited (ISBN 81-203-1601-0) (2000).

108. A. Macková, V. Havránek, V. Švorčík, N. Djourelov, and T. Suzuki, *Degradation of PET, PEEK and PI induced irradiation with 150 keV Ar^+ and 1.76 MeV He^+ ions*, Nucl. Instrum. Methods Phys. Res. B. **240**, 245 (2005).

109. A. Taniike, N. Kubota, M. Takeuchi, Y. Furuyama, and A. Kitamura, *Ion-irradiation induced hydrogen loss from polyethylene film*, J. Appl. Phys. **92**, 6489 (2002).

110. E.H. Lee, *Ion-beam modification of polymeric materials-fundamental principles and applications*, Nucl. Instrum. Methods Phys. Res. B **151**, 29 (1999).